Effects of Concentration, Crystal Structure, Magnetism, and Electronic Structure Method on First-principles Oxygen Vacancy Formation Energy Trends in Perovskites

Matthew Curnan[†,‡] and John R. Kitchin[*,†,¶]

National Energy Technology Laboratory-Regional University Alliance (NETL-RUA), US Department of Energy, P.O. Box 10940, Pittsburgh, Pennsylvania 15236

E-mail: jkitchin@andrew.cmu.edu

Phone: +1 (412) 268-7803. Fax: +1 (412) 268-7139

[*]To whom correspondence should be addressed

[†]National Energy Technology Laboratory-Regional University Alliance (NETL-RUA), US Department of Energy, P.O. Box 10940, Pittsburgh, Pennsylvania 15236

[‡]Department of Materials Science and Engineering, Carnegie Mellon University, 5000 Forbes Ave, Pittsburgh, PA 15213

[¶]Department of Chemical Engineering, Carnegie Mellon University, 5000 Forbes Ave, Pittsburgh, PA 15213

Abstract

Systematic prediction of the redox reaction energetics of large sets of $3d$ transition metal oxides is imperative to the selection of oxygen carrier candidates in applications ranging from chemical looping to solid oxide fuel cell (SOFC) cathode design. In particular, the energetic study of oxygen vacancy formation in unmixed perovskites with La, alkali, and alkaline A-site metal cations – as well as $3d$ transition metal B-site cations – is a crucial first step in understanding the energetic tunability afforded by cation doping in ABO_3 materials. An assessment of the relative oxygen vacancy formation energetics of LaBO$_3$, SrBO$_3$, and similar materials that serve as a guideline for predicting energetics in related systems is completed below using Density Functional Theory (DFT). This assessment illustrates which simplifications can be made in the prediction of energetics trends without affecting trend order. The independent consideration of oxygen vacancy concentration, crystal structure, and anti-ferromagnetic (AFM) magnetism revealed that these factors in DFT calculations had no effect on trend order. However, ferromagnetic (FM) SrBO$_3$ trend order was affected between $SrMnO_3$ and $SrFeO_3$ as a function of defect concentration. Moreover, energetic trends were also formed by adding constant, incremental values of the Hubbard U parameter contributed to the $3d$ orbitals of perovskite B-sites. calculation of U parameters using linear response theory or by a literature review of previous research.

Keywords: transition metal oxide, oxygen defect, redox energy, DFT+U, ferromagnetism, anti-ferromagnetism

Introduction

Transition metal perovskite (ABO_3) oxides are used in applications that include gas sensors,[1,2] photovoltaics,[3] spintronics and other forms of magnetic coupling,[4,5] exhaust gas CO[6,7] and NO_x[8–10] treatment, and steam reformation.[11,12] In the context of redox reactivity, these oxides are utilized in two primary fields of research, namely clean energy and

catalysis. With respect to clean energy, transition metal oxides function as cathode materials to improve the oxygen reduction reaction (ORR) kinetics of solid oxide fuel cells (SOFCs),[13,14] while they serve as oxygen carriers in chemical looping combustion (CLC) processes[15,16] intended for applications in power generation coupled with carbon capture and storage (CCS).[16–18] Particular to chemical looping processes, unmixed oxygen carriers possess strong theromdynamic properties, enabling effective redox reactivity in various physical implementations of such processes.[12,16,19] Though their oxygen transport properties are characteristically poor relative to this level of reactivity,[16] the mixture of cations on several of the sites of these oxygen carriers has been demonstrated to improve oxygen transport properties significantly without significantly lowering redox reactivity.[19–21] With respect to catalysis, mixed-metal perovskite solutions are frequently used to tune and optimize operating parameters in hydrocarbon oxidation processes[19,22] including fuel conversion,[6,23,24] CO_2 selectivity,[25] and specific surface area[25,26] relative to other reaction parameters. Perovskite (ABO_3) materials, which contain at least two different types of metal cations located at two distinct (A and B) sites in a stoichiometric 1:1 concentration ratio, have material properties that are readily tuned by mixing cation compositions on either their A or B-sites.[12,19,21] The mixture of structurally similar solid-state materials with different compositions, which can incorporate large sets of cation combinations in ABO_3 materials, is capable of optimizing material properties pertinent to SOFCs such as conductivity[20,27,28] and oxygen diffusion[20,29] as a function of conditions such as temperature[14] or strain.[13] Furthermore, perovskites such as (La,Sr)MnO_3 (LSM) and (La,Sr)MnO_3 (LSF) are also chemically stable over a wide range of redox reaction conditions[21,30] and are compatible with multiple substrate support materials such as yttria-stabilized zirconia (YSZ) and alumina (Al_2O_3).[16,18]

LaBO$_3$ materials with B-site cations comprised of 3d transition metals with partially filled d-shells (B = Sc–Cu) have favorable structural,[9,24,31] electronic,[7,16] and catalytic[11,32,33] properties over the range of thermodynamic temperature[34,35] and pressure[36,37] conditions appropriate for redox reaction applications.[17,25,38,39] In redox applications, these LaBO$_3$ ma-

terials must observe not only favorable bulk and surface redox reactivity, but also favorable ionic and electronic migration properties.[12] The transport of oxygen anions and electrons from bulk to surface facilitates the transformation between energetically stable bulk and surface structures containing oxygen vacancies, allowing the mechanisms of surface and bulk oxygen vacancy formation to cooperatively contribute to redox reactivity.[12,21] In these mechanisms, the facile reduction and oxidation of $3d$ transition metal B-sites located on the perovskite surface is enabled by their multiple available valence states, allowing local conservation of charge in the presence of substantial surface oxygen vacancy concentrations.[35,40] Many LaBO$_3$ materials observe favorable oxygen transport properties, such as consistently low migration energies associated with oxygen diffusion from surface to bulk,[35,41] displacement of A and B-site cations away from the diffusion paths of oxygen, the presence of several open diffusion paths between different oxygen crystallographic sites, and sufficient concentrations of mobile oxygen anions.[21] Thus, for LaBO$_3$ materials favoring oxygen transport, the attainment of equilibrium concentrations of oxygen vacancies (or oxygen storage capacities) significant for redox applications should be determined primarily by limitations in thermodynamic redox reactivity rather than by limitations in oxygen migration.[12]

Further improvements in perovskite redox reactivity can be achieved by doping the A-site composition, which features the rare earth metal La^{+3} in these materials, with alkali (Na, K, etc.) or alkaline (Sr, Ca, etc.) metals bearing lower +1 or +2 oxidation states, respectively.[8,42] The stoichiometric ABO$_3$ BO$_2$-terminated surface can be oxidized via doping with cations that have lower oxidation states, weakening bonds between that surface and adsorbed oxygen.[43] This bond weakening facilitates oxygen vacancy formation, enabling the preservation of charge neutrality[44] at sufficiently high reaction temperatures and low oxygen partial pressures.[45] Considering the size and predictability of oxygen migration energies and the varied property enhancements afforded to ABO$_3$ materials by solid-state mixing, the precise estimation of oxygen vacancy formation energies in both bulk and surface ABO$_3$ perovskites is critical to selecting suitable catalyst and oxygen carrier candidates tuned for

specific catalysis, SOFC, and chemical looping applications.

Experimental efforts engaged in the process of selecting metal oxides for applications are not currently aided by a comprehensive set of guidelines assessing the effects of A-site or B-site mixed metal oxide tuning on redox reactivity, since computations encompassing the entire spectrum of unmixed ABO_3 compositions have not yet been completed.[46] Therefore, we aspire to resolve a portion of those computations comparing the oxygen vacancy formation energies of perovskites, employing a methodology that is able to determine which characteristics of those materials must minimally be considered to yield reliable energetic trends in calculations involving unmixed A-site (A = La, Sr, Ba, K) and B-site (B = Sc–Cu) ABO_3 compositions. In all of these energetic calculations, oxygen vacancy formation is defined from the following redox reaction for a supercell consisting of n unit cells, with n equal to the inverse of the stoichiometric level of oxygen deficiency (δ):[18,20,35]

$$nABO_3 \rightarrow nABO_{3-\frac{1}{n}} + \frac{1}{2}O_2(g) \tag{1}$$

Even though a comprehensive set of calculations encompassing the entire range of partially filled $3d$ transition metal B-sites has not yet been completed, previous work has used first-principles, Density Functional Theory (DFT) methods to calculate energetic trends comparing oxygen vacancy formation energies or related formation energies of bulk and surface ABO_3 materials that share an A-site composition. Several studies that incorporated these bulk[46,47] and surface[48] energetic trends evaluated the entire range of $3d$ transition metal B-sites over multiple A-sites while employing various structural, magnetic, and electronic simplifications to the calculation of the ABO_3 electronic structure and reactivity. In those studies, essentially monotonic trends were observed in vacancy formation energies. Other studies employed advanced electronic structure methods to more accurately calculate the vacancy formation energies of a narrower range (B = V–Fe) of LaBO$_3$ materials while modeling only the most common structural and magnetic states observed under most experimentally viable redox reaction conditions.[35] One of the most comprehensive studies of vacancy for-

mation energy evaluated a small LaBO$_3$ B-site range (B = Mn–Ni) while also considering structural and magnetic features. The features considered were consistent with ABO$_3$ systems under various experimental conditions. The electronic structures of these systems were calculated using DFT+U.[34] However, the U parameters utilized in that prior work were derived from fitting structural and energetic parameters to experimental formation energy data.[34] This fitting approach cannot be used on new perovskite systems for which reliable experimental data is not available. The selection of ABO$_3$ candidates for energy and catalysis applications requires the existence of an extensive data set of consistently calculated vacancy formation energies, one that will likely include candidates for which prior specific experimental results do not exist.

As indicated in previous work, the electron self-interaction error is known to produce non-systematic errors in the DFT energetic properties of transition metal oxides.[49] The Hubbard U method can correct on-site electron self-interaction in the $3d$ and $4f$ orbitals of transition metal cations and La, respectively. In this context, the responses of pertinent orbital occupancy matrices to linear perturbations can be implemented to calculate effective, theoretically rigorous U values.[50,51] The errors affecting transition metal oxides consist of both systematic and non-systematic contributions, the former of which results from O_2 molecular overbinding. This overbinding leads to overestimation of the O_2 molecule DFT energy, introducing a constant offset that systematically affects all DFT resolved energetic properties involving O_2.[49,52] The non-systematic errors in formation energies resulting from electron self-interaction are partially corrected with the introduction of Hubbard U parameters selected via linear response.[49,51]

In this work we aim to examine the effects of the simplifying approximations employed in previous studies[34,35,47,48] on energetic trends in oxygen vacancy formation energies. These previous studies have broadly focused on inducing singular, relatively high vacancy concentrations in cubic perovskite crystal structures, evaluating magnetism to a limited extent and assessing electronic structure with either solely standard exchange and correlation function-

als or with corrective Hubbard U parameters derived from fitting to experimental data. Each of these approximations may affect the trends in oxygen vacancy formation energy, thus we determine the effects of including them in this work.

The first approximation addressed in this study, which was featured in previous studies,[34,35,47,48] is the consideration of a singular high oxygen vacancy defect concentration in energetic calculations. Even under a constant set of experimental conditions, different materials will have different equilibrium vacancy concentrations,[18,20] though these could be much lower than what is convenient to calculate using first-principles methods under certain conditions. To address these experimental and computational limitations, we have calculated vacancy formation energies at several constant levels of vacancy concentration, determining whether the trends would change at different defect concentrations.

The second factor considered in the evaluation of oxygen vacancy formation energy trends is the perovskite crystal structure. Though undistorted cubic perovskites are seen in experiments and are simple to model,[34] orthorhombic and rhombohedral Jahn-Teller (J-T) distortions of the unit cell resulting from changes in B-site electron configurations are more commonly observed under most experimental conditions of interest.[34,53] Furthermore, the impacts of strain or, in mixed metal solid-state solutions, cation ordering on bulk cubic ABO_3 can also induce rhombohedral or orthorhombic distortions with out-of-phase rotation of adjacent unit cells along the pseudocubic [100], [010], and [001] axes.[54,55] In this work, we have computed oxygen vacancy formation energies for the rhombohedral and orthorhombic crystal structures in addition to the cubic structure to assess the importance of structure on studied energetic trends.

A systematic investigation of the effects of magnetism on oxygen vacancy formation energies in perovskites has not been performed before. Perovskites may observe various magnetic states, including non-magnetic (NM),[34] paramagnetic (PM),[35] ferromagnetic (FM), and antiferromagnetic (AFM) states depending on temperature and pressure.[34] Each of these magnetic states can demonstrate different energetics, potentially affecting the observed energetic

trends. In this work, the ferromagnetic (FM) and anti-ferromagnetic (AFM) states commonly observed across the perovskites reviewed in this study are uniformly applied across all systems characterized by energetic trends.[34,56,57] Considering that prior first-principles studies of $LaMnO_3$ required that magnetism, J-T distortion, and other factors be studied simultaneously to resolve formation energy results accurately with respect to experiments, oxygen vacancy concentration dependence and crystallographic symmetry distortions will be considered simultaneously with magnetism.[58,59] Finally, the simplifying approximation of not attempting to correct spurious electron correlation effects in $3d$ transition metal oxides is addressed by applying the Hubbard U model to characterize electron self-interaction across ABO_3 of interest, applying U parameter corrections to the $3d$ orbitals of all B-sites studied and the $4f$ orbitals of La. This method, chosen for its computational efficiency[60] and successfully demonstrated in previous studies to smaller ranges of $LaBO_3$ and $SrBO_3$ materials,[34,35] will be employed to assess changes in energetics using linear response derived U parameter values.[50,51]

Methods

VASP calculations

Unless otherwise stated, DFT calculations were performed using the Vienna Ab-initio Simulation Package (VASP 5.2.12).[61,62] The Perdew-Burke-Ernzerhof (PBE) parameterization of the Generalized Gradient Approximation (GGA)[63] was used to account for electron exchange and correlation. Pseudopotentials generated by the Projected Augmented Wave (PAW)[64] method were used. The default PAW pseudopotentials provided by VASP were used for all atoms. Typical computational parameters characteristic of a plotted set of calculations completed in this study are a 550 eV plane-wave energy cutoff, a $6 \times 6 \times 6$ Monkhorst-Pack[65] k-point sampling mesh set with respect to the perovskite unit cell (containing 5, 10, or 20 atoms in this study), and a 0.02 eV/Å force tolerance on each atom for structural relaxation

calculations.

For all structures, ground state lattice parameters and DFT total energies (E_0) were determined by first performing multiple fixed cell volume, variable cell shape and atomic coordinate structural relaxation calculations encompassing their corresponding ground state equilibrium cell volumes (V_0). The resulting total energies from those calculations were fitted with the Birch-Murnaghan equation of state.[66] This fitting procedure was performed for perovskite structures that contained no vacancy defects (ABO_3) and one vacancy defect ($ABO_{3-\delta}$), in which δ refers to the fraction of oxygen atoms removed from a structure by the formation of a vacancy. The fractional level of oxygen deficiency or deviation from stoichiometric ABO_3 (δ) induced by oxygen vacancy formation, in which oxygen deficiency leads to reduction of the B-site cation, is related to the number of oxygen sites substituted by vacancy defects normalized with respect to the ABO_3 unit cell.[67] Oxygen vacancy formation energies (ΔE_{vac}) were calculated using Equation 2 for supercell systems consisting of n unit cells ($\delta = 1/n$):[49,68]

$$\Delta E_{vac}(eV/O) = nE_{ABO_{3-\frac{1}{n}}} + \frac{1}{2}E_{O_2} - nE_{ABO_3} \quad (2)$$

In the expression above, values of ΔE_{vac} are referenced with respect to the DFT total energy of the gaseous diatomic oxygen molecule (E_{O_2}) in its triplet ground state,[68,69] which is systematically corrected by a factor of 1.36 eV/O_2 to account for the overbinding of molecular O_2 in all ΔE_{vac} calculations.[49]

Vacancy concentration

In previous work, we focused on energetic trends in reactions involving oxygen that utilized small, computationally convenient unit cell representations of perovskites.[48] When these energetic trends involve oxygen vacancy formation in cubic perovskites, an oxygen vacancy removes one of the three oxygens in the $1 \times 1 \times 1$ ABO_3 unit cell. This vacancy concentration is very high. Vacancy formation energy trends obtained at such high vacancy concentrations

may not be representative of trends observed at lower vacancy concentrations. Whether vacancy concentration has a significant impact on ΔE_{vac} trends was determined by creating single oxygen vacancies in $1 \times 1 \times 2$, $2 \times 2 \times 1$, and $2 \times 2 \times 2$ cubic supercells consisting of 10, 20, and 40 atoms, respectively. These supercells correspond to levels of oxygen deficiency (δ) of 0.5, 0.25, and 0.125 and are proportional to the fractions of vacancies in respective supercells by a factor $\delta/3$. With respect to experimental oxygen storage capacities,[15,18,20,70] these values of δ are more realistic than the value of $\delta = 1$ found in the case of the ABO_3 cubic unit cell.

Crystal structure

In this work, we assess the significance of crystal structure on the trends in oxygen vacancy formation energies. The cubic ABO_3 structure frequently experiences J-T distortions affecting its octahedral shell tilt angles or axial bond lengths. These distortions lead to phase transitions from the cubic to rhombohedral or cubic to orthorhombic phases, respectively.[34] The temperature and pressure conditions under which a particular structural phase of an ABO_3 material is thermodynamically favorable vary with A-site and B-site cation composition.[71,72] Under conditions typical of redox reaction applications,[34] experimental results featuring $LaBO_3$ have shown that bond lengthening, orthorhombic distortions tend to be favorable when B-site d-band filling is lower, while rotational or rhombohedral distortions are generally more favorable as d-band filling increases.[53] In $LaMnO_3$, cubic, rhombohedral, and orthorhombic phases are all experimentally observed under typical reaction conditions.[72] Therefore, it is important to understand whether the trends in the oxygen vacancy formation energy in simple cubic perovskite structures are representative of the trends in the other perovskite polymorph structures.

Across all A-site and B-site compositions studied, we computed the oxygen vacancy formation energies of the relaxed rhombohedral and orthorhombic structural phases and compared them to the relevant energies of cubic structures. The initial atomic coordinates

provided to all structurally relaxed, rhombohedrally distorted perovskites are derived from the 10 atom $\sqrt{2}\times\sqrt{2}\times\sqrt{2}$ unit cell of $LaCoO_3$, which observes $R\overline{3}c$ crystallographic symmetry.[73] For all orthorhombic structures studied, the 20 atom $\sqrt{2}\times\sqrt{2}\times 2$ unit cell of $LaCrO_3$ provides corresponding initial atomic coordinates.[74] In all calculations employing orthorhombic structures, the *Pbnm* crystallographic symmetry, which is an alternate setting for the *Pnma* space group achieved by permuting its a and b axes, was used. The oxygen vacancy formation energies resulting from inducing vacancies at both non-equivalent site symmetric oxygen positions, namely the $4c$ and $8d$ positions, were tested in the orthorhombic case.[75]

Magnetism

When considering the lower portion of the range of temperature ($\approx$ 700 K) conditions at which redox reactions can occur, the ground state structures of some A-site and B-site compositions of ABO_3 – primarily those with B = Mn, Fe, and Co – have different magnetic states.[34,71] The effects of including magnetism on ΔE_{vac} ordering are resolved by investigating the oxygen vacancy formation energies of ferromagnetic (FM) and anti-ferromagnetic (AFM) perovskite configurations.[34] In $2\times2\times2$ cubic perovskites, G-type, A-type, and C-type AFM states were evaluated across several $LaBO_3$ that could be directly compared to experimental results (B = V–Mn), whereas in smaller supercells that cannot geometrically represent these magnetic orderings due to periodic limits, magnetic moment ordering was rendered to resemble G-type anti-ferromagnetism.[56,57] All calculations involving magnetism incorporate collinear spin polarization and correct the exchange correlation functional with the Vosko-Wilk-Nusair interpolation,[76] while all magnetic moments imposed on studied perovskites were allowed to relax.[57]

DFT+U: Preliminary evaluation

In GGA calculations involving $3d$ transition metal oxides or other strongly correlated systems, shortcomings in modeling the electronic structures of these systems frequently lead to

non-systematic errors in their formation energies.[49,50,77] The Hubbard U model was selected to account for this on-site electron-electron interaction error characteristic of strongly correlated systems investigated using GGA. This method balances computational expense with the ability to largely correct energetic trends developed from these systems.[60,78,79] When applied across several strongly correlated systems of varying composition, values of U calculated by the Hubbard model cannot be treated as parameters fitted to experimental data, for U values represent the intrinsic, system dependent responses to perturbing particular orbital occupations.[51,80]

The accurate determination of the correct magnitudes of these intrinsic responses is time consuming and resource intensive. Therefore, in order to gain broad insight into the impacts of adding U values with varying magnitudes to ΔE_{vac} ordering on multiple systems, energetic trends sharing constant values of U are derived for the perturbation of pertinent orbital occupations. These orbital occupations include the $3d$ orbitals of the ABO_3 B-site and the $4f$ orbitals of the La A-site cation. When evaluating the effects of perturbing the $4f$ orbitals of LaBO_3, U_{4f} values ranging from 0-12 eV in 1 eV increments were surveyed; the upper limit of that range was taken from studies that attempted to minimize the differences between experimentally observed and DFT resolved band structures for several La containing compounds.[81,82] With respect to perturbation of the B-site $3d$ orbitals of perovskites with La and Sr A-site compositions, U_{3d} values ranging from 0-8 eV in 0.5 eV increments were evaluated for ΔE_{vac} ordering changes; the selection of this range was based on previous ABO_3 perturbation response calculations.[83,84] Spin polarized calculations applying the rotationally invariant Dudarev implementation of the Hubbard U model were performed on PM perovskites[35] to complete this preliminary evaluation using VASP and the previously detailed calculation criteria. In this Hubbard U implementation, the on-site Coulombic (U) and Exchange (J) terms are combined into a single effective U parameter (U_{eff}) to account for errors in exchange correlation as implemented in VASP.[85]

DFT+U: Linear response

After obtaining broad insights on the effects of U value selection in VASP, an analysis supplementing the previous section was performed using the Quantum Espresso (version 5.0.1) software package over several LaBO$_3$ and SrBO$_3$ systems while considering both PM and FM magnetic states.[86] This subsequent analysis, after comparison to its analogue completed in VASP, is used to provide first-principles estimates of U parameter values and determine whether changes in ΔE_{vac} ordering are likely. In order to determine whether several of these changes in ΔE_{vac} ordering are actually predicted to occur, U values are calculated from the initial (χ_0) and final (χ) linear responses that result from perturbing the on-site $3d$ orbital occupations of several relevant PM LaBO$_3$ (B = V, Cr, Mn, Fe) materials.[51,86] In other cases, such as LaCoO$_3$ and LaNiO$_3$, estimated theoretically determined U values will be taken from previous papers.[83,84] In each linear response calculation, the initial guesses for A-site, B-site, and O atom input U values (U_{in}) are all set to 0 eV, while initial structural information is estimated from a procedure detailed in the Supporting Information section. Therefore, even though these calculations are initialized using electronic structure information provided largely from GGA rather than GGA+U ground states, changes in the structure of the material induced by addition of the U parameter are handled approximately.[80] From this adaptation of the linear response method, initial (χ_0) and final (χ) response matrices are derived to yield final calculated U values (U_{out}) via Equation 3:[80]

$$U_{out} = \chi_0^{-1} - \chi^{-1} \tag{3}$$

Calculations involving the Hubbard U model following the preliminary DFT+U evaluation were performed with the default semi-core valence state Vanderbilt Ultrasoft pseudopotentials provided by the Quantum Espresso package.[86] Determination of U_{out} values from linear response was completed using a 8 × 8 × 8 Monkhorst-Pack[65] k-point sampling mesh set with respect to a 40 atom 2 × 2 × 2 ABO$_3$ cubic supercell, as well as a 50 Ry plane-wave

energy cutoff. Initial structural information calculated for U parameter estimation derived from Quantum Espresso were obtained using a 50 Ry energy cutoff, a $8 \times 8 \times 8$ k-point sampling mesh set with respect to a 5 atom cubic ABO_3 unit cell, and a force tolerance of 0.001 Ry/Bohr (approximately 0.026 eV/Å) on each atom. The Birch-Murnaghan equation of state was used to estimate values of E_0 and V_0 in a procedure matching that used to yield ΔE_{vac} values in VASP.[66] Gaussian occupation spreading was applied to all Quantum Espresso calculations. In all linear response calculations, spreading values were minimized to obtain linear perturbation behavior, while a constant 0.01 Ry spreading was applied to all Quantum Espresso calculations that involve achieving structural information. In this study, the combined effects of t_{2g} and e_g orbital occupancy anisotropy and spin state on the on-site Coulombic terms forming the traces of the final response matrices are not considered, thus orbital occupancies are not decomposed and are considered separately using Löwdin orthonormal atomic wavefunctions. This simplification has been applied successfully in previous studies involving similar materials.[83,84] Furthermore, the same U_{out} values derived from linear response calculations on bulk ABO_3 materials are applied to ABO_3 and $ABO_{3-\delta}$ structures. Within the current study, $3d$ U parameter contributions resulting from perturbation of the A-site and O valence shell occupancies in ABO_3 materials, which would be performed in the presence of B-sites providing much larger contributions to relevant U parameters, are also ignored.

Results and Discussion

In previous work, energetic trends involving surface oxygen adsorption and oxygen vacancy formation reactions were calculated for (001) oriented, BO_2 terminated, 1×1 unit cell surface representations of perovskite materials while varying A-site (A = La and Sr) and B-site (B = Sc-Cu) compositions using Vanderbilt Ultrasoft pseudopotentials.[48] As shown in Figure 1, we observe similar trends when using PAW-PBE pseudopotentials to characterize oxygen

vacancy formation in bulk perovskite structures. Both sets of trends are characteristically monotonic when considered from high to low d-band filling of the B-site over an A-site dependent B-site range, with a reversal in energetic ordering occurring beyond this range of d-band filling. Furthermore, comparable energetic results have been observed over the same sets of materials when investigating related energetic properties such as oxygen migration energy.[87]

Given that the alteration of B-site valence charge accommodates oxygen vacancy formation in ABO_3 materials,[35,40] the likely cause for the loss of monotonicity in vacancy formation energy trends at low d-band fillings is insufficient valence charge provided by B-site $3d$ electrons to energetically stabilize stoichiometric ABO_3 with respect to oxygen-deficient $ABO_{3-\delta}$. In perovskites with B-sites that have largely filled $3d$ transition metals, instability of the ABO_3 phase is also observed in the form of negative ΔE_{vac} values for materials such as $KCuO_3$. Note that these negative ΔE_{vac} values, as well as all ΔE_{vac} values illustrated in the figures shown in this paper, are derived using an oxygen molecule reference energy (-4.25 eV) that has been corrected using the results provided in Wang et al.[49] Thus, any prediction of whether particular ΔE_{vac} values are positive or negative will be implicitly affected by errors in this correction. Though the correction to O_2 molecular overbinding[49] observed in GGA calculations can impact ΔE_{vac} magnitudes, energetic instability in these materials results from the inability of the combination of A-site and B-site valence charges to balance the negative charge of oxygen in principle. This can occur when elements such as Cu cannot adopt sufficiently high valence charges to thermodynamically stabilize KBO_3 as B-site cations in experiment.[88]

The results shown in Figure 1 were obtained with the goal of predicting trends in ΔE_{vac} ordering encompassing a broad set of ABO_3 compositions while minimizing computational cost. In accomplishing this goal, several simplifying approximations were made to the calculations performed, including a high oxygen vacancy concentration (small unit cell), highly symmetric cubic crystal structure, not considering magnetism, and using standard GGA cal-

culations. Therefore, subsequent sections of this study are devoted to assessing the impact of considering the effects of these simplifying approximations, addressing their individual and combined influences on ΔE_{vac} ordering over B-site ranges of interest. The results of evaluating these simplifying approximations can be easily extended to ABO_3 with A-site compositions containing any alkali or alkaline metal, as well as possibly transition and rare earth metals, given the energetic similarity of trends possessing the same valence states.

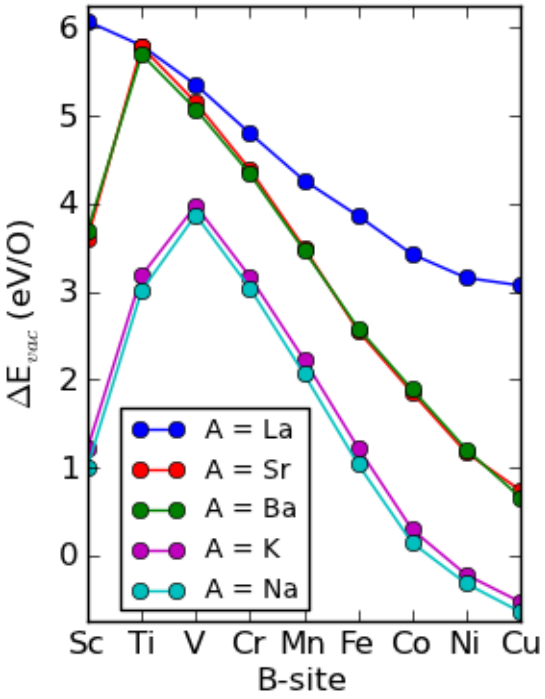

Figure 1: Oxygen vacancy formation energy trends across cubic unit cell representations of perovskite materials with A = La, Sr, Ba, K, and Na. Note that perovskites with A-sites containing alkali and alkaline metals hold monotonic trend ordering over the same B-site ranges and possess very similar ΔE_{vac} values, inferring that the A-site cation contributes little to differentiating ABO_3 energetic trends outside of its variable valence state.

Vacancy concentration

When performing formation energy calculations on the five atom cubic ABO_3 unit cell, forming a single oxygen vacancy leads to very high oxygen vacancy concentrations, in which one of every three oxygen sites is substituted by a vacancy. In previous work,[48,89] $1 \times 1 \times 1$

unit cell ABO_3 representations were used to calculate energetic trends, ignoring the possible dependence of oxygen vacancy concentration on these trends. Therefore, we address the limitations of our previous research by calculating ΔE_{vac} trends over $3d$ transition metal perovskites with La and Sr A-sites at lower oxygen vacancy concentrations. The vacancy formation energy for a single oxygen vacancy in $1\times1\times2$, $2\times2\times1$, and $2\times2\times2$ cubic supercells were calculated, with one vacancy out of every six, twelve, or twenty-four oxygen atoms with a vacancy. In our calculations, we observed an apparent oxygen vacancy concentration dilute limit of one vacancy per 24 oxygen sites ($\delta = 0.125$) based on the convergence of ΔE_{vac} values with decreasing vacancy concentration observed in previous studies of $LaAlO_3$.[90]

As shown in Figures 2 and 3, trends in ΔE_{vac} trends are largely conserved, with the most significant changes occurring at the end points. The vacancy formation energies tend to converge with increasing unit cell size, generally becoming easier to form. For both A-site compositions, constituent ΔE_{vac} values of the unit cell ($1 \times 1 \times 1$) trend are significantly different from those derived from supercell structures, which tend to have closer ΔE_{vac} values. Furthermore, at particular B-sites, such as Sc in both $LaBO_3$ and $SrBO_3$ systems, changes in ΔE_{vac} values with increasing supercell size can be abrupt and large. These larger changes in ΔE_{vac} values can likely be attributed to the removal of vacancy self-interaction error with increasing supercell size. Vacancy self-interaction error, which occurs when single vacancies spuriously interact with themselves in periodically repeated $ABO_{3-\delta}$ structures, is removed when each supercell spatial dimension consists of more than solely the unit cell, for adjacent periodically repeated cells no longer share the same vacancy in ABO_3 supercells.[91] We conclude that vacancy concentration can have a significant effect on the magnitude of the formation energy, but apart from the end points, especially for B-sites with very few d-electrons, the overall trends do not change significantly. The endpoint effects have been previously observed and explained in terms of a lack of outer electrons available for bonding.[89]

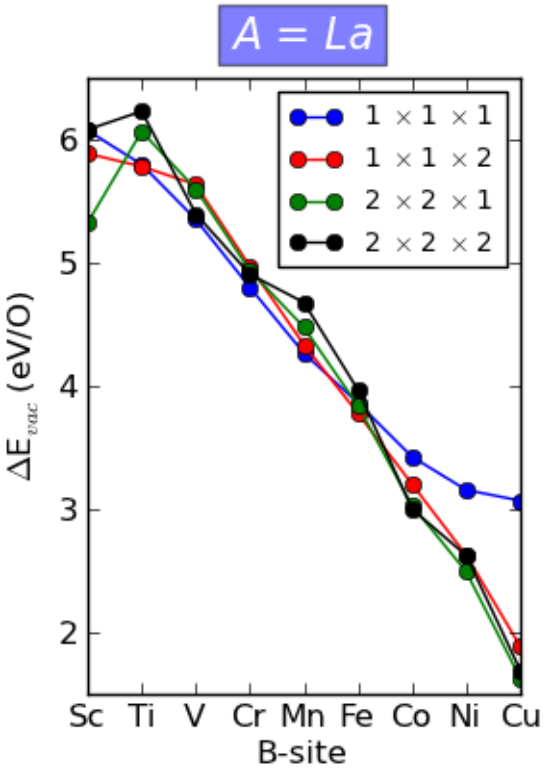

Figure 2: Oxygen vacancy formation energy trends across cubic supercell representations of perovskite materials with La A-site composition and dimensions $1 \times 1 \times 1$, $1 \times 1 \times 2$, $2 \times 2 \times 1$, and $2 \times 2 \times 2$. Though vacancy formation energy convergence with vacancy dilution is observed in some LaBO$_3$ systems, such convergence is less uniform than that seen in corresponding SrBO$_3$ systems.

Crystal structure

We next consider oxygen vacancy formation energies in rhombohedral ($R\bar{3}c$) and orthorhombic ($Pbnm$) distortions to the cubic perovskite structure. The effect of rhombohedral distortion is studied by directly comparing the 10 atom $R\bar{3}c$ unit cell to a corresponding 10 atom $1 \times 1 \times 2$ cubic supercell, while similarly comparing the 20 atom $Pbnm$ supercell to a $2 \times 2 \times 1$ cubic supercell. As shown in Figures 4 and 5, similar trends are observed in cubic ABO_3 and either rhombohedrally or orthorhombically distorted ABO_3, respectively. Furthermore, when comparing energetic trends of different crystallographic representations of ABO_3 that share the same A-site composition, the relative differences between adjacent ΔE_{vac} values are similar across trends. In the case of orthorhombic distortions involving

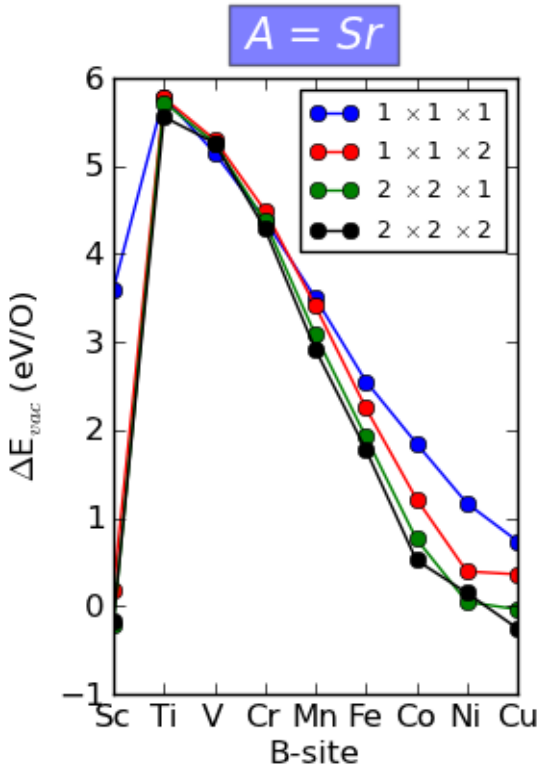

Figure 3: Oxygen vacancy formation energy trends across cubic supercell representations of perovskite materials with Sr A-site composition and dimensions $1 \times 1 \times 1$, $1 \times 1 \times 2$, $2 \times 2 \times 1$, and $2 \times 2 \times 2$. In addition to preserving trend ordering, almost all of the actual values of ΔE_{vac} values of particular systems consistently converge with increasing oxygen vacancy defect dilution.

the 20 atom $\sqrt{2} \times \sqrt{2} \times 2$ *Pbnm* unit cell, oxygen vacancies can be induced at two non-equivalent oxygen sites: at the 4*c* and 8*d* Wyckoff positions.[75] In Figure 5, results involving vacancy formation only at the 8*d* Wyckoff position are depicted. However, as shown in the Supporting Information section, ΔE_{vac} ordering is entirely preserved regardless of the site at which oxygen vacancies are induced. For example, at each LaBO$_3$, the comparison of ΔE_{vac} values corresponding to vacancies created at either oxygen site reveals that their magnitudes are similar within a 0.13 eV tolerance. This tolerance is below the energetic criterion of 0.2 eV used to determine the relative significance of each contribution to oxygen vacancy formation energies in Lee et al.,[34] illustrating that studies calculating results at a similar level of precision would have ignored the contribution of considering different oxygen sites to energetics.

Though the results shown in Figure 4 were produced from structural relaxations initialized with experimental atomic coordinates from the $R\bar{3}c$ $LaCoO_3$ structure,[73] $LaCrO_3$ and $LaMnO_3$ were provided with alternate coordinates in separate calculations to evaluate the effects of varying both the magnitude of the rhombohedral distortion and unit cell size. For both $LaCrO_3$ and $LaMnO_3$, this was accomplished by scaling the initialized $LaCoO_3$ reduced coordinates such that they were consistent with the lattice constants and rhombohedral angles of pertinent experimental structures resolved at typical redox reaction conditions.[92] Considering that numerous independent sources confirm nearly identical lattice constants for orthorhombic $LaCrO_3$,[53,74,93] alternate atomic coordinates were not provided to any orthorhombic structures. Despite significant changes in initial guesses of atomic structure, the relaxed ground state energies of all structures employing alternate atomic coordinates or lattice parameters were identical to their conventional coordinate analogues within a 0.003 eV tolerance. This energetic similarity illustrates that the existence of particular cubic ABO_3 structural distortions, rather than their initial magnitudes, contributes primarily to the increases in ΔE_{vac} values shown in Figures 4 and 5. In both figures, these increases are largely uniform, causing ΔE_{vac} values to be uniformly higher. Thus, oxygen vacancy formation is less favorable in rhombohedrally and orthorhombically distorted ABO_3. Nevertheless, when comparing these distorted ABO_3 to corresponding cubic structures containing the same number of atoms, the total DFT energies of stoichiometric ABO_3 are uniformly lower in the distorted phases than the cubic phase, indicating that structural distortions are thermodynamically favorable at 0 K. When considering these two observations and evidence of the removal of structural distortions at higher redox reaction temperatures,[34,35,71] the link between increasing oxygen vacancy formation and higher reaction temperatures appears to largely result from the phase transitions characteristic of these perovskite systems under redox reaction operating conditions. Lastly, neither the 10 atom $R\bar{3}c$ ($\sqrt{2} \times \sqrt{2} \times \sqrt{2}$) nor the 20 atom $Pbnm$ ($\sqrt{2} \times \sqrt{2} \times 2$) unit cells feature any spatial dimension in which oxygen vacancies are unphysically shared between periodically repeated $ABO_{3-\delta}$ structures. There-

fore, these results should not be significantly affected by vacancy defect self-interaction and evaluating supercell representations of these structures is less important than equivalently evaluating cubic structures.[91]

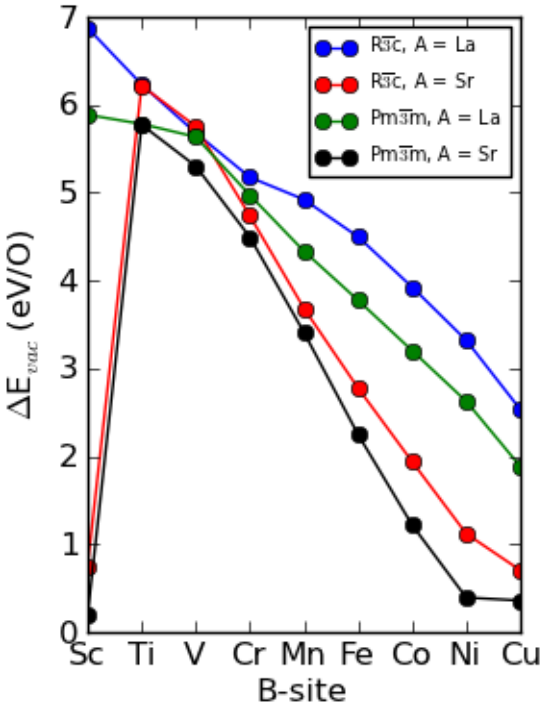

Figure 4: Oxygen vacancy formation energies in 10 atom rhombohedral ($R\bar{3}c$ unit cell) and cubic ($Pm\bar{3}m$ supercell) perovskite crystal structures. Across almost all systems studied, vacancy formation is more favorable in SrBO$_3$ and cubic systems rather than LaBO$_3$ and rhombohedral systems.

Magnetism

In previous studies, trends in oxygen vacancy formation energy were calculated while neglecting spin-polarization and magnetism in both bulk[35,47] and surface[48] calculations. Previous research has also indicated that correct characterization of the relative energetics of 3d transition metal perovskites, namely LaMnO$_3$[58,59] and LaVO$_3$,[94] can only be accomplished when jointly considering magnetism, J-T distortions, and other factors simultaneously. The most common forms of magnetism observed in LaBO$_3$ and related materials are ferromagnetism

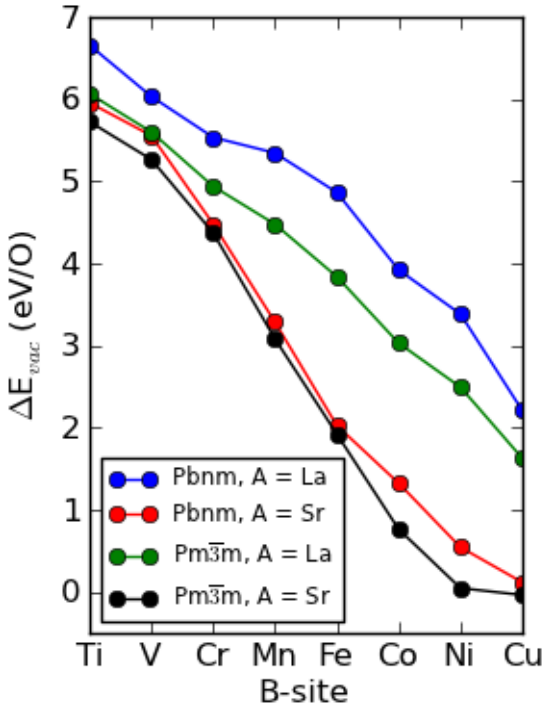

Figure 5: Oxygen vacancy formation energies in 20 atom orthorhombic ($Pbnm$ unit cell) and cubic ($Pm\bar{3}m$ supercell) perovskite crystal structures. The relative differences between adjacent systems in energetic trends is shared by systems with the same A-site, with vacancy formation once again being more favorable in SrBO$_3$ and cubic systems than in LaBO$_3$ and orthorhombic systems.

(FM) and anti-ferromagnetism (AFM).[34,57] The analyses completed for all FM materials, as shown in Figures 6 and 8, and AFM materials, as illustrated in Figures 7 and 9, accounts for all previously mentioned factors by reevaluating the effects of oxygen vacancy concentration dependence and crystallographic symmetry for all LaBO$_3$ and SrBO$_3$. Review of Figure 6 reveals that ΔE_{vac} ordering is largely conserved over the entire range of B-sites regardless of oxygen vacancy concentration or supercell size in the FM cubic supercell, while evaluation of rhombohedrally distorted FM LaBO$_3$ characterized by the $R\bar{3}c$ unit cell supports the same conclusion, albeit at higher ΔE_{vac} values. However, in cubic supercells consisting of 20 atoms or greater ($2 \times 2 \times 1$), the ΔE_{vac} of LaVO$_3$ drops abruptly and significantly, leading to a change in ΔE_{vac} ordering between LaTiO$_3$ and LaCrO$_3$. Similarly, in the FM SrBO$_3$ results pictured in Figure 8, ΔE_{vac} ordering is conserved in all tested systems consisting of fewer

than 20 atoms, including the 10 atom systems based on the $R\bar{3}c$ unit cell. For systems – such as the $2 \times 2 \times 1$ cubic supercell or the $\sqrt{2} \times \sqrt{2} \times 2$ *Pbnm* unit cell – in which the number of atoms in the ABO_3 structure is 20 or greater, ΔE_{vac} ordering changes between $SrCrO_3$ and $SrFeO_3$, as the ΔE_{vac} of $SrMnO_3$ decreases with increasing oxygen vacancy concentration dilution.

Across all studied $LaBO_3$ and $SrBO_3$ in which an abrupt ΔE_{vac} change does not occur as a function of vacancy concentration, the relative ΔE_{vac} values of trends representing systems that share the same number of atoms – or oxygen vacancy concentrations – are highly similar. The two most salient examples of this feature are visualized in Figure 8; they are realized by comparing the $1 \times 1 \times 2$ cubic energetic trend with the corresponding $R\bar{3}c$ trend (10 atom systems) and the $2 \times 2 \times 1$ cubic trend with its orthorhombic *Pbnm* analogue (20 atom systems). In both comparisons, energetic trends that share the same number of atoms observe not only have the same ΔE_{vac} ordering, but also the same relative ΔE_{vac} values, as seen most apparently at the ΔE_{vac} ordering change between $SrCrO_3$ and $SrFeO_3$. Even though the lower symmetry rhombohedral (10 atom) and orthorhombic (20 atom) systems have universally higher energies of vacancy formation than their cubic analogues, visual inspection reveals that the relative amounts by which the ΔE_{vac} of $SrMnO_3$ is greater than or less than that of $SrFeO_3$ is almost entirely unaffected by changes in crystal structure.

In contrast, when an abrupt change in ΔE_{vac} ordering occurs, such as that seen in the case of $2 \times 2 \times 1$ cubic $LaVO_3$ and its constituent energetic trend, the lower symmetry *Pbnm* energetic trend agrees with the ΔE_{vac} ordering indicated in cubic trends featuring higher oxygen vacancy concentration rather than the $2 \times 2 \times 1$, 20 atom cubic trend with which it can be directly compared. Both FM $LaBO_3$ and $SrBO_3$ cases show a clear oxygen vacancy concentration dependence with respect to ΔE_{vac} ordering over particular systems. However, previous theoretical work has indicated that the correct energetics of $LaVO_3$ can only be obtained in DFT when jointly considering J-T distortion and magnetism,[94] while experimental results indicate that axial J-T distortion in $LaVO_3$ structures is stable un-

494 der redox reaction temperature and pressure conditions.[53] As a result, the conservation of
495 ΔE_{vac} ordering shown in the higher cubic LaBO$_3$ oxygen vacancy concentrations and the
496 *Pbnm* structure is probably a more accurate representation of results that would be observed
497 in experiment than the order switching seen in lower oxygen vacancy concentration cubic
498 structures. Therefore, the ΔE_{vac} ordering change observed in cubic FM $LaVO_3$ is likely an
499 artifact of an oversimplified first-principles model. In contrast, the gradual change in ΔE_{vac}
500 ordering observed in $SrMnO_3$, which is validated by trends that assume a different crystal-
501 lographic symmetry, is likely an accurate representation of particular experimental results.
502 Nevertheless, theoretical efforts to characterize FM $SrMnO_3$ reveal that this magnetic state
503 is generally only stable when inducing large epitaxial strains (4.5-4.9%) to $SrMnO_3$ surfaces.
504 Thus, under the vast majority of viable redox reaction conditions, this magnetic state is not
505 energetically accessible and ΔE_{vac} ordering would remain conserved.[4]

506 In contrast to the FM structures studied, ΔE_{vac} ordering remained conserved across all
507 $1 \times 1 \times 2$ and $2 \times 2 \times 1$ LaBO$_3$ and SrBO$_3$ structures, as shown in Figures 7 and 9. However,
508 a cubic supercell consisting of at least 8 B-site cations – or a $2 \times 2 \times 2$ supercell – is required
509 to fully represent the geometries of distinctly different AFM ordering types (A, C, and G).[56]
510 Previous experimental results aggregated in a first-principles study of AFM LaBO$_3$ (B =
511 Ti–Fe) materials are used as a reference to assess the ability of simplified cubic $2 \times 2 \times 2$ super-
512 cells to predict – for each studied system – the most energetically favorable type of magnetic
513 ordering and the magnetic moment magnitudes of those energetically favorable systems.[57]
514 In all studied FM and AFM structures, relaxed magnetic moments on the d-orbitals of
515 B-site cations were significantly greater than 0 and other magnetic moment contributions
516 only within the B-site cation range B = V–Ni, while the strongest magnetic moments were
517 generally observed in compounds containing Fe, Mn, or Co B-sites. Unlike other studied
518 structures, AFM $LaFeO_3$ observed strong axial distortion upon structural relaxation, which
519 would, according to previously derived results involving geometrically distorted ABO_3 ma-
520 terials, likely increase ΔE_{vac} by a non-systematic amount. As a result, comparing AFM

$LaFeO_3$ with other $2 \times 2 \times 2$ cubic AFM structures directly via an energetic trend is not possible in our model. Considering the limitations of data available for reference to experiment, the B-site range in which magnetic moments are significantly present, and the axial distortion of AFM $LaFeO_3$, only $2 \times 2 \times 2$ AFM $LaVO_3$, $LaCrO_3$, and $LaMnO_3$ are studied here. Consistent with both previous experimental and DFT results, the C-type AFM state is most favorable in $LaVO_3$ and the G-type state is favored in $LaCrO_3$. In contrast to experimental results albeit in agreement with previous DFT results, C-type AFM is predicted to be the most energetically favorable $LaMnO_3$ magnetic state, as opposed to A-type AFM. The total AFM magnetic moments calculated for $LaVO_3$, $LaCrO_3$, and $LaMnO_3$ (C-type) are 1.44, 2.58, and 3.44, respectively; all magnetic moments are in good agreement with reference results.[57] As shown in Figure 7, AFM structures modeled in accordance with past experimental results that account for the energetically favorable magnetic orderings of different materials still conserve ΔE_{vac} ordering. The difference between the ΔE_{vac} of C-type and A-type $LaMnO_3$ of 0.4 eV is small with respect to the generally observed ΔE_{vac} differences between materials located adjacent to one another on the same trend. Though this energetic difference between different magnetic types could be significant when the ΔE_{vac} values of adjacent members of an energetic trend are close, such as the small energetic differences observed between FM $SrMnO_3$ and FM $SrFeO_3$ at some dilute oxygen vacancy concentrations, the AFM energetic trends derived generally feature large energetic differences between adjacent oxides and would thus remain unaffected by considering different AFM states.

DFT + U

Effect of U on oxygen vacancy formation energy

In our final section, we first consider the effect of correcting for $3d$ electron-electron interaction error in $LaBO_3$ and $SrBO_3$ systems by systematically introducing Hubbard U parameters over large B-site ranges that form oxygen vacancy formation energy trends. Considering the close proximity of several empirically fitted values of U derived in past studies[34] and our

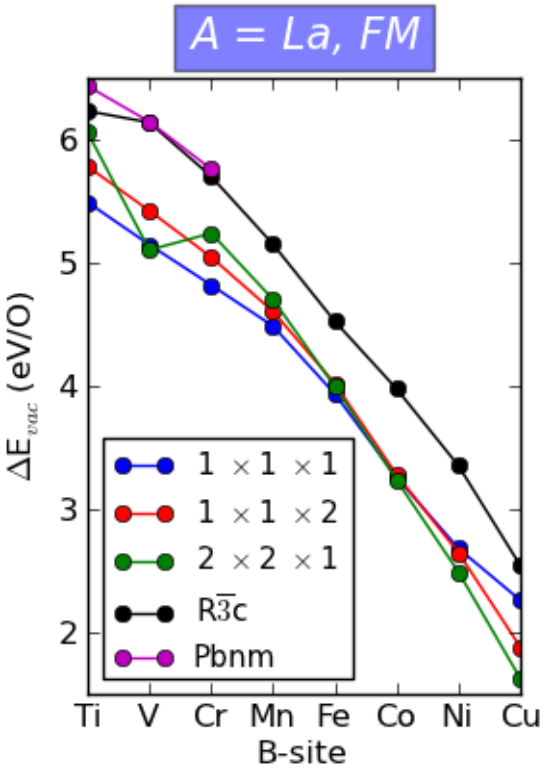

Figure 6: Oxygen vacancy formation trends for ferromagnetic LaBO$_3$ perovskites in cubic supercells of increasing size (as well as increasing oxygen vacancy dilution), as well as rhombohedral and orthorhombic unit cells. The 10 atom rhombohedral unit cell can be directly compared to the $1 \times 1 \times 2$ cubic supercell, while the 20 atom orthorhombic unit cell is analogous to the $2 \times 2 \times 1$ cubic supercell.

overarching goal of determining the impact of U value magnitude on ΔE_{vac} ordering over entire trends, we initially evaluate energetic trends sharing constant values of U. The effect of adding a U parameter to the La $4f$ orbitals of LaBO$_3$ materials is not readily apparent, as the $4f$ orbitals are highly localized though nearly empty. When examining this effect, we varied U from 0 to 12 eV in 1 eV increments, computing trends in vacancy formation energy associated with constant values of U shared over the entire trend. As shown in Figure 10, applying U to the La $4f$ orbitals has no significant effect on the formation energies, likely due to the near emptiness of the La $4f$ orbitals in the +3 oxidation state of La. Consideration of these effects in Sr is unnecessary, as Sr has no occupied f-orbitals.

When evaluating the effects of adding U to the $3d$ orbitals of LaBO$_3$ and SrBO$_3$ B-sites, all systems considered are spin-polarized, though magnetic moments are not imparted to

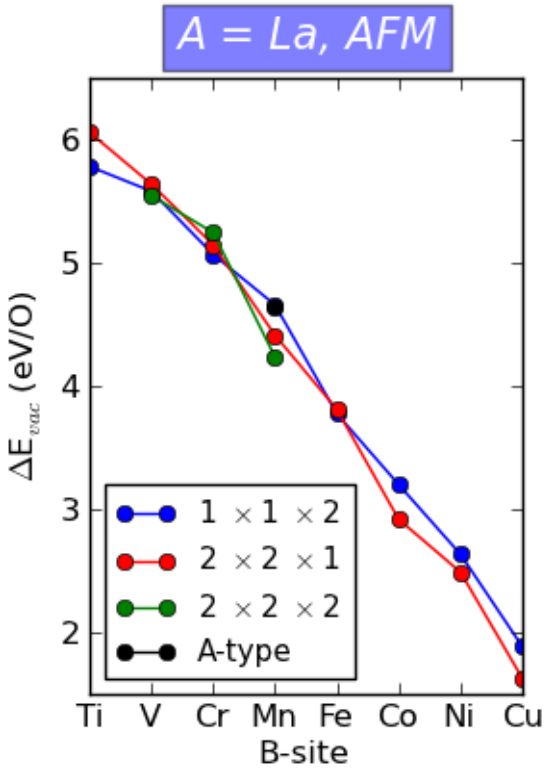

Figure 7: Oxygen vacancy formation trends for antiferromagnetic LaBO$_3$ perovskites in cubic supercells of increasing size and thus decreasing oxygen vacancy concentration. The $2 \times 2 \times 2$ energetic trend links the most favorable structures with respect to first-principles calculations of oxygen vacancy formation and stability of the ABO$_3$ structure, namely C-type LaVO$_3$, G-type LaCrO$_3$, and C-type LaMnO$_3$. The single point not connected to a trend represents A-type LaMnO$_3$, which is experimentally predicted to be the most favorable AFM state of LaMnO$_3$.

atoms in any of these systems. Thus, our examination of the effects of adding U to $3d$ transition metals investigates paramagnetic (PM) ABO$_3$ systems, as these systems are most often encountered at the temperature and pressure conditions necessitated by applications of interest to our study.[35,84] In evaluating these effects, U parameters between 0 and 8 eV separated by 0.5 eV increments are employed as constants to form energetic trends that evaluate ΔE_{vac} ordering. ΔE_{vac} values that are directly relevant to illustrating ordering changes are visualized as energetic results in two figures. As shown in Figure 11, three changes in ΔE_{vac} ordering are predicted to occur across LaBO$_3$ systems, occurring between the V-Cr, Mn-Fe, and Co-Ni B-site cation pairs. In particular, the Mn-Fe cation pair ordering change is consistent with previous first-principles research and experimental data.[34,35]

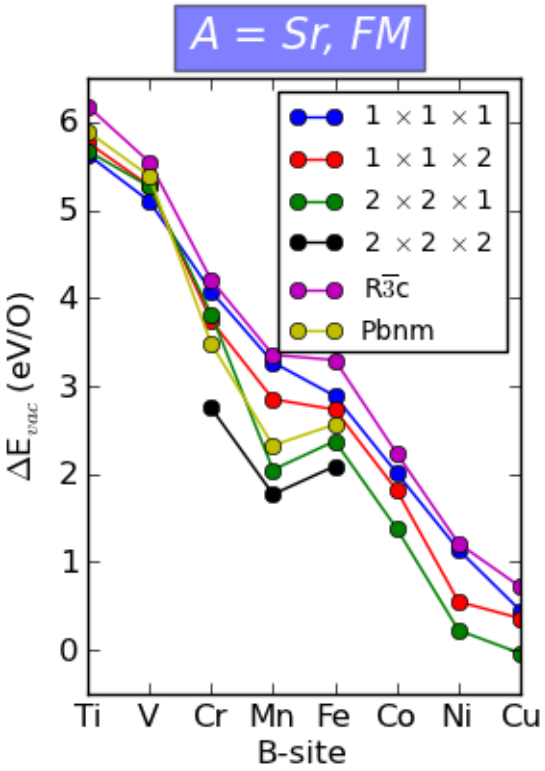

Figure 8: Oxygen vacancy formation trends for ferromagnetic SrBO$_3$ perovskites in cubic cells of successively decreasing vacancy concentration, as well as corresponding trends for rhombohedral and orthorhombic unit cells. Once again, the 10 atom rhombohedral unit cell can be directly compared to the $1 \times 1 \times 2$ cubic supercell, while the 20 atom orthorhombic unit cell is analogous to the $2 \times 2 \times 1$ cubic supercell.

The ΔE_{vac} ordering changes that occur between the LaVO$_3$-LaCrO$_3$ and LaMnO$_3$-LaFeO$_3$ pairs are both seen between U values of 3.5 and 4.0 eV, while the LaCoO$_3$-LaNiO$_3$ ΔE_{vac} ordering change is observed in the slightly higher 4.0-4.5 eV range. A similar ΔE_{vac} ordering change between the SrCoO$_3$-SrNiO$_3$ pair is found at approximately 6.0 eV when evaluating SrBO$_3$ systems, as is shown in Figure 12. This similar energetic feature observed when evaluating both LaBO$_3$ and SrBO$_3$ systems is most likely a result of the significant ΔE_{vac} reduction contributed by the spin-polarized Co atom in the spin exchange-splitting inclusive Dudarev implementation of GGA+U.[85] In addition, a unique SrCrO$_3$-SrMnO$_3$ ordering change occurs in the 4.0-4.5 eV range in SrBO$_3$ trends. Even though Figures 11 and 12 illustrate only a fraction of the constant U values across which ABO$_3$ systems were tested, all tested U values between 0 and 8 eV revealed that no additional ΔE_{vac} ordering changes be-

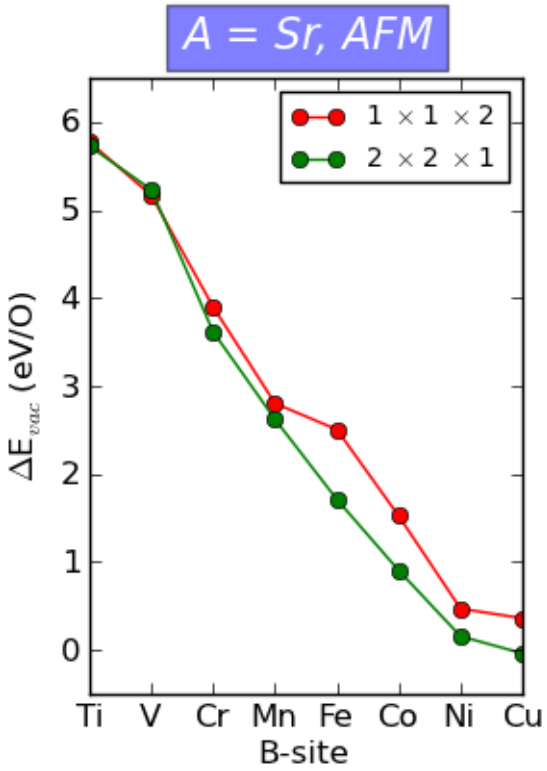

Figure 9: Oxygen vacancy formation trends for antiferromagnetic SrBO$_3$ perovskites formed from the cubic unit cell and $1 \times 1 \times 2$ cubic supercell structures.

yond those pictured occurred and that none of the ΔE_{vac} ordering changes became reversed when successively higher U values were imposed on the trends containing them. Instead, these ΔE_{vac} ordering changes generally became more pronounced with increasing U.

One key difference between the changes in ΔE_{vac} ordering in LaBO$_3$ systems versus SrBO$_3$ systems is the apparent cause of the ordering changes. In the case of LaBO$_3$ systems, one ABO$_3$ involved in a ΔE_{vac} ordering change is largely responsible for that change, as is found in the significant decrease of LaVO$_3$, the increase of LaFeO$_3$, and the decrease of LaCoO$_3$ with increasing U. In contrast, ΔE_{vac} ordering changes in SrBO$_3$ systems appear to result from both the decrease in ΔE_{vac} of an ABO$_3$ with less B-site d-band filling and the corresponding increase in ΔE_{vac} of an adjacent system with more B-site d-band filling, as is seen in SrCrO$_3$ and SrMnO$_3$. In evaluating the possible ΔE_{vac} ordering changes observed in LaBO$_3$ and SrBO$_3$ systems while estimating threshold values of U at which ordering changes occur, subsequent analysis can focus solely on assigning appropriate values of U to systems

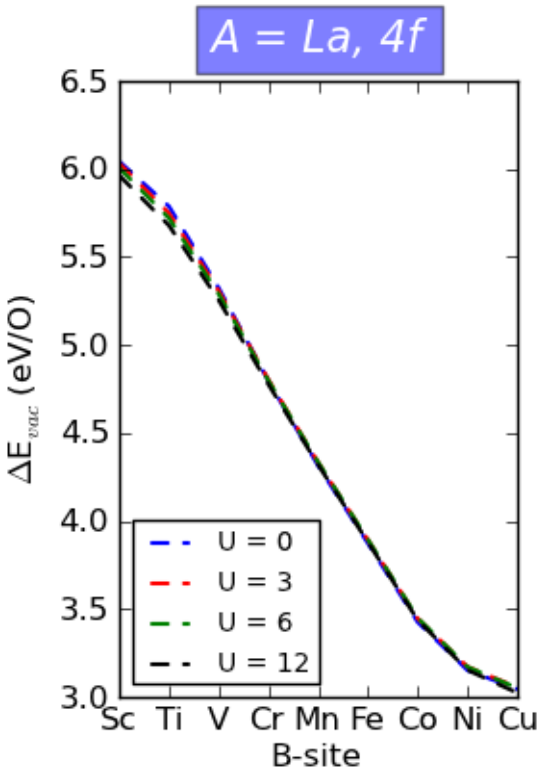

Figure 10: Applying Hubbard U parameters to the La $4f$ orbitals of LaBO$_3$ systems does not significantly affect the oxygen vacancy formation energy trend linking them for any potentially physically relevant values of U.

explicitly involved in ΔE_{vac} ordering changes.

Linear response U

In order to reliably predict whether ΔE_{vac} ordering changes between two systems positioned adjacent to one another on an energetic trend actually occur, U values for the $3d$ orbitals of ABO$_3$ B-sites involved in ΔE_{vac} ordering changes were systematically computed, determining whether the calculated U values are near the U values at which ordering changes occur. One way to achieve this is to systematically select U values using the first-principles methodology of linear response theory.[51] Using the Vanderbilt Ultrasoft pseudopotentials provided by the Quantum Espresso software package, the linear response approach is used to calculate several U parameters for systems involved in ΔE_{vac} ordering changes. As shown in Table 1, values of the Gaussian spreading needed to minimally induce linear behavior in the orbital occupations

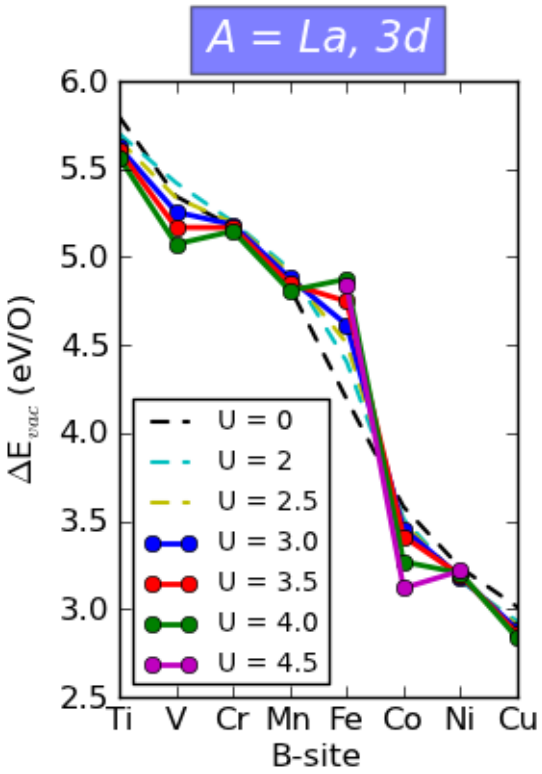

Figure 11: Increasing the values of U contributed to the $3d$ orbitals of B-sites of systems incorporated into LaBO$_3$ oxygen vacancy formation energy trends reveals distinct changes in ΔE_{vac} ordering between LaVO$_3$-LaCrO$_3$, LaMnO$_3$-LaFeO$_3$, and LaCoO$_3$-LaNiO$_3$. Solid trend lines indicate the U constants between which any ΔE_{vac} ordering changes on the trend occur.

of the initial and final components of the linear response were derived for each system and initially performed at equilibrium cell volumes. These equilibrium cell volumes are represented by cubic lattice constants (a) that correspond to the GGA ground states found in Quantum Espresso. Though these ground state volumes are generally consistent across both the VASP and Quantum Espresso software packages, the cell volumes of tabulated paramagnetic (PM) systems changed differently when transitioning from GGA ($U = 0.0$ eV) to GGA+U ($U = 7.0$ eV) ground states across VASP and Quantum Espresso. Given the relationship between the uniform expansion and contraction of atomic positions (changes in cell volume) and total energy when using DFT+U,[95] this discrepancy between how energetic calculations in both software packages are affected by the addition of a U parameter can cause error, as the resolved U parameters from one package are used to draw conclusions from the

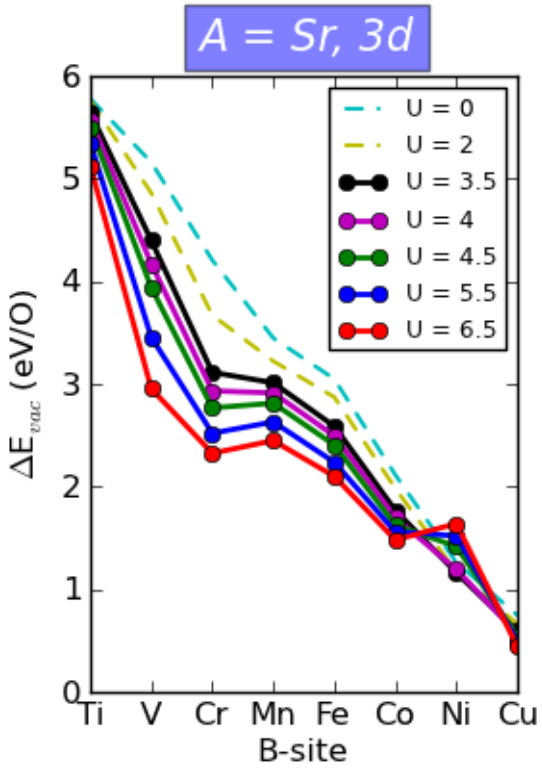

Figure 12: Increasing the values of U contributed to the $3d$ orbitals of B-sites of systems incorporated into $SrBO_3$ oxygen vacancy formation energy trends reveals distinct changes in ΔE_{vac} ordering between $SrCrO_3$-$SrMnO_3$ and $SrCoO_3$-$SrNiO_3$. Solid trend lines indicate the U constants between which any ΔE_{vac} ordering changes on the trend occur. Due to the gradual changing of ΔE_{vac} ordering at $SrCoO_3$-$SrNiO_3$ and the closeness of their ΔE_{vac} values between 5.5 and 6.5 eV, only trend lines with $U = 5.5$ and 6.5 eV are visualized above.

formation energetics of another. In order to illustrate the extent to which this cross-platform related error could affect predictions of energetic ordering, U parameters of three systems – $LaCrO_3$, $LaMnO_3$, and $LaFeO_3$ – were calculated at lattice constants corresponding to both their GGA ground state cell volumes (shown in Table 1) largely shared across VASP and Quantum Espresso and their GGA+U ground state cell volumes derived in VASP.

For $LaCrO_3$, $LaMnO_3$, and $LaFeO_3$, lattice constants (a) increased from 3.84 to 3.97, 3.82 to 3.95, and 3.81 to 3.94 Å when transitioning from GGA to GGA+U ground states, respectively. This is equivalent to the introduction of approximately 3.5% tensile strain in each case. When applying lattice constants corresponding to the GGA+U ground state volumes detailed above, the linear response U of $LaCrO_3$ decreased from 10.7 to 10.2 eV,

that of $LaMnO_3$ increased from 8.4 to 8.9 eV, and the U of $LaFeO_3$ increased from 7.0 to 7.4 eV. These contrasting results achieved in systems with different cell volumes illustrates the sensitivity of resolved U parameters with respect to structural effects such as strain while illustrating the potential for using results achieved in Quantum Espresso to validate findings in VASP. This shows that U can be affected by positive or negative errors resulting from cell volume expansion equal to as much as 0.5 eV in cross-platform comparisons involving these systems. Nevertheless, the relatively low magnitude of this error margin with respect to the differences between linear response U parameters and their corresponding ΔE_{vac} ordering changes strongly suggests that the $LaVO_3$-$LaCrO_3$ and $LaMnO_3$-$LaFeO_3$ ordering changes do occur, while the $SrCrO_3$-$SrMnO_3$ ordering change likely occurs.

Table 1: Linear response derived U parameter values on the $3d$ orbitals of perovskite *B*-sites corresponding to systems at which changes in ΔE_{vac} ordering could possibly occur, along with the minimum Gaussian spreading values needed to achieve linear perturbation behavior in each system and the cubic lattice constants (a) at which the GGA ground states of the U values shown were derived.

Perovskite	Spreading	a (Å)	U (eV)
$LaVO_3$	0.035	3.88	6.2
$LaCrO_3$	0.020	3.84	10.7
$LaMnO_3$	0.030	3.82	8.4
$LaFeO_3$	0.035	3.81	7.0
$SrCrO_3$	0.030	3.81	6.6
$SrMnO_3$	0.030	3.80	7.7

Previous work[34,35] supports the presence of the $LaMnO_3$-$LaFeO_3$ ΔE_{vac} ordering change using different experimental and first-principles methods. A further review of literature indicates that, for the predicted PM low spin or intermediate spin (LS/IS)[35] state of $LaCoO_3$, a self-consistent linear response U value of 7.0 eV has already been calculated,[84] while a corresponding value of $U = 5.7$ eV has been calculated for $LaNiO_3$.[83] Therefore, the $LaCoO_3$-$LaNiO_3$ ΔE_{vac} ordering change most likely occurs, although validation of this prediction would require our replication of these calculated U values under a common set of assumptions and parameters that could be applied to any $LaBO_3$ system involved in our derived

energetic trends. Therefore, the correction of electron-electron interaction in the $3d$ orbitals of perovskite B-sites likely affects both LaBO$_3$ and SrBO$_3$ ΔE_{vac} trend order.

Though the ΔE_{vac} trend ordering changes found previously most likely occur due to the high magnitudes of U parameters derived from linear response theory and literature review and the relatively low magnitudes of predicted ordering changes, more precise U values can be resolved by testing the simplifying assumptions under which the U parameters themselves were calculated. Several of these assumptions have already been mentioned, such as the decomposition of t_{2g} and e_g orbital occupancy terms into separate response matrices using Löwdin orthonormal atomic wavefunctions for systems possibly observing high orbital occupancy anisotropy, such as SrNiO$_3$.[83] The assumption to ignore A-site and O contributions to the $3d$ U parameters of ABO$_3$ materials, as well as the assumption that U parameters calculated for ABO$_3$ can be applied to ABO$_{3-\delta}$ systems on the same redox reaction coordinate,[78] have also been mentioned or alluded to previously. In addition, there are several more assumptions beyond those already mentioned that can be addressed. As shown in previous systems involving transition metal oxides,[96] the use of a self-consistent approach in the linear response method can produce U values that are significantly different from those resolved without a self-consistent approach. Thus, neglecting to use the self-consistent approach in calculating U values via linear response theory constitutes an assumption. Furthermore, the use of Vanderbilt Ultrasoft pseudopotentials in Quantum Espresso to derive U values for energetic calculations performed in VASP using PAW-PBE pseuodopotentials, though completed in past studies for similar materials,[83] should be tested to establish the comparability of redox reaction results derived using different software packages and pseudopotential sets.

A comparison of several U values previously derived via experimental fitting for LaBO$_3$ and SrBO$_3$ systems with Ultrasoft[46] and PAW-PBE[34] pseudopotentials shows that differences in the U parameter results resolved using two different pseudopotential sets can be as high as 1.0 eV. Given that ΔE_{vac} ordering change predictions in our study are formed from energetic trends of constant U separated by increments of 0.5 eV (in the case of B-site U

parameters correcting $3d$ electron-electron interaction), transferring U parameters between different software packages and pseudopotential sets constitutes a significant assumption. Another assumption made in our current study is ignoring the coupled effects of different forms of magnetism and the introduction of U on ΔE_{vac} ordering, despite the prevalence of PM states in ABO_3 systems under typical redox reaction conditions.[35] In particular, the $SrMnO_3$-$SrFeO_3$ ΔE_{vac} ordering change occurring in FM systems would produce a significant effect on ΔE_{vac} ordering that could manifest itself in lower temperature and pressure applications of ABO_3 systems. By addressing these assumptions and others in our U parameter selection, we can apply appropriate values of U to oxygen vacancy formation energetic calculations that will verify the conditions under which ΔE_{vac} ordering changes are predicted to occur.

Summary and Conclusions

In evaluating the effects of including several structural, magnetic, and electronic simplifications on the energetic ordering of ΔE_{vac} trends formed from perovskites that share an A-site cation and span large ranges of $3d$ transition metal B-site cations, we find that ΔE_{vac} trend ordering can be affected by accounting for magnetic and electronic simplifications. Structural simplifications reviewed in this study, which were considered due to their variability under temperature and pressure conditions pertinent to applications of interest, were found to not affect the ΔE_{vac} trend ordering when considered independent of other simplifications. Considering that oxygen vacancy concentration varies under reaction conditions relevant to our study, we first investigated the effect of diluting vacancy concentration on ΔE_{vac} trend ordering and find that $LaBO_3$ and $SrBO_3$ energetic trends remain unaffected by changes in oxygen vacancy concentration. Therefore, $LaBO_3$ and $SrBO_3$ redox reaction energy order is not a function of defect concentration when the bulk equilibrium concentration of defects is considered independent of other simplifications. Given that the cubic crystallo-

graphic symmetry of perovskite materials is frequently distorted to form orthorhombic and rhombohedral phases under pertinent reaction conditions, the effect of considering alternate crystallographic phases on ΔE_{vac} trend ordering was investigated by evaluating the energetic trends formed by the experimentally observed $Pbnm$ and $R\bar{3}c$ structures, respectively. When considering crystal structure independent of other simplifications, no changes in the ΔE_{vac} trend ordering of LaBO$_3$ and SrBO$_3$ were observed across energetic trends sharing the same phase. However, the ΔE_{vac} trends of orthorhombically and rhombohedrally distorted LaBO$_3$ and SrBO$_3$ possessed nearly universally higher ΔE_{vac} values than their direct cubic analogues despite the universal favorability of these distorted structures when they contained no oxygen vacancies, inferring that oxygen vacancy formation is significantly less energetically favorable in all studied non-cubic perovskites.

The investigation of magnetic simplifications in LaBO$_3$ and SrBO$_3$ was completed by reviewing both FM and AFM structures, varying crystallographic symmetry and oxygen vacancy concentration across all FM ABO$_3$ and testing sample A-type, C-type, and G-type AFM structures. In all tested AFM cases, no significant changes in ΔE_{vac} trends were observed. However, when employing the cubic crystal structure approximation to FM energetic trends, ΔE_{vac} ordering changes were observed at LaVO$_3$-LaCrO$_3$ and SrMnO$_3$-SrFeO$_3$. In the case of the FM LaBO$_3$ ordering change, reevaluation of the energetic trend of structures surrounding the ΔE_{vac} ordering with the more experimentally accurate $Pbnm$ structure revealed that the abrupt ΔE_{vac} ordering change surrounding LaVO$_3$ was likely an artifact of employing the cubic structural simplification. In contrast, a more extensive analysis of the FM SrBO$_3$ energetic trend revealed that the ΔE_{vac} ordering change at SrMnO$_3$ was a function of oxygen vacancy concentration and occurred independent of crystal structure considerations.

Lastly, when performing an initial investigation of the effect of accounting for electron-electron interaction in LaBO$_3$ and SrBO$_3$ energetic trends, the Hubbard U model was employed by assigning several values of U to the $3d$ orbitals of ABO$_3$ B-sites and the $4f$ orbitals

of La in LaBO$_3$ systems. When assigning U values of increasing magnitude to the $4f$ orbitals of La in LaBO$_3$, LaBO$_3$ ΔE_{vac} trend order remained unchanged. However, similar assignment of U values to the $3d$ orbitals of PM LaBO$_3$ revealed ΔE_{vac} trend order changes between $LaVO_3$-$LaCrO_3$, $LaMnO_3$-$LaFeO_3$, and $LaCoO_3$-$LaNiO_3$ between U = 3.5-4.5 eV, while corresponding assignment of U to SrBO$_3$ resolved ΔE_{vac} trend order changes between $SrCrO_3$-$SrMnO_3$ in the range U = 4.0-4.5 eV and $SrCoO_3$-$SrNiO_3$ at approximately 6.0 eV. Calculation of U values derived by a linear response approach indicated that the $LaVO_3$-$LaCrO_3$ and $LaMnO_3$-$LaFeO_3$ ΔE_{vac} trend ordering changes almost certainly can happen, while a review of literature U values reveals that the $LaCoO_3$-$LaNiO_3$ ΔE_{vac} ordering change likely occurs and further calculations reveal that the $SrCrO_3$-$SrMnO_3$ ordering change also likely occurs.

In conclusion, the results directly resolved in this study can be generalized to yield a broader set of principles that can be applied to energetic trends involving similarly structured metal oxide systems. When evaluating energetic trends that are formed from systems with similar oxygen vacancy defect concentrations or crystal structures, variations in concentration or structure across those energetic trends will more likely produce nearly constant shifts in them rather than changing the relative ordering of specific systems within them. Therefore, when investigating solely the relative energetic ordering of systems within a trend, oxygen vacancy concentration and crystal structure simplifications can be made outside of exceptional circumstances.

In contrast, the effects of different types of magnetism on energetic trends cannot be conclusively generalized to the extent that a single simplification can characterize them. In order to evaluate the relative energetic ordering of a particular set of magnetic systems, trends involving supercells of increasing size must be evaluated to determine the extent to which magnetism non-systematically affects energetics. Therefore, when attempting to characterize relative ordering in energetic trends over a particular set of reaction conditions, the forms of magnetism that can affect systems both within those trends and over those

conditions should be accounted for prior to their study.

After using information concerning magnetism to form a basis for relative energetic ordering in trends, the study of non-systematic, theoretical effects on energetics can proceed, starting with the consideration of electronic structure method. When used to model electronic structure, the Hubbard U model accounts for potentially spurious electron-electron interactions using procedures that can be incremental in their provision and predictive in their ability to assess energetics. Given that the primary expected contribution to non-systematic, theoretical error in an energetic trend is related to electron-electron interaction error, the Hubbard U method can be used to determine whether accounting for electron-electron interaction affects energetic ordering. This can be accomplished by first determining which systems within that trend observe changes in energetic ordering upon being subjected to incrementally larger values of an appropriate U value, subsequently using a predictive method to resolve values of U for systems in which changes in ordering are observed, and finally comparing the two results to predict ordering in energetic trends.

DISCLAIMER

This project was funded by the Department of Energy, National Energy Technology Laboratory, an agency of the United States Government through a support contract with URS Energy & Construction Inc. Neither the United States Government nor any agency thereof, nor any of their employees, nor URS Energy & Construction, Inc., nor any of their employees, makes any warranty, expressed or implied, or assumes any legal liability or responsibility for the accuracy, completeness, or usefulness of any information, apparatus, product, or process disclosed, or represents that its use would not infringe privately owned rights. Reference herein to any specific commercial product, process, or service by trade name, trademark, manufacturer, or otherwise, does not necessarily constitute or imply its endorsement, recommendation, or favoring by the United States Government or any agency thereof. The

views and opinions of authors expressed herein do not necessarily state or reflect those of the United States Government or any agency thereof.

Acknowledgement

As part of the National Energy Technology Laboratory's Regional University Alliance (NETL-RUA), a collaborative initiative of the NETL, this technical effort was performed under the RES contract DE-FE0004000. The authors of this paper also thank Dr. Heather Kulik for her contributions to discussions involving the use of the Hubbard U method in this article. The computing resource used to complete this paper was provided by Carnegie Mellon University and its Department of Chemical Engineering.

Supporting Information Available

A complete database of the results from this work with examples of using the data to generate the figures are provided in the supporting information. This material is available free of charge via the Internet at `http://pubs.acs.org/`.

References

(1) Fossdal, A.; Menon, M.; Wærnhus, I.; Wiik, K.; Einarsrud, M.-A.; Grande, T. Crystal Structure and Thermal Expansion of $La_{1-x}Sr_xFeO_{3-\delta}$ Materials. *J. Am. Ceram. Soc.* **2004**, *87*, 1952–1958.

(2) Alexandrov, V.; Piskunov, S.; Zhukovskii, Y. F.; Kotomin, E. A.; Maier, J. First-Principles Modeling of Oxygen Interaction with $SrTiO_3$(001) Surface: Comparative Density-Functional LCAO and Plane-Wave Study. *Integr. Ferroelectr.* **2011**, *123*, 10–17.

(3) Qi, T.; Curnan, M. T.; Kim, S.; Bennett, J. W.; Grinberg, I.; Rappe, A. M. First-

principles Study of Band Gap Engineering via Oxygen Vacancy Doping in Perovskite $ABB'O_3$ Solid Solutions. *Phys. Rev. B* **2011**, *84*, 245206:1–6.

(4) Lee, J. H.; Rabe, K. M. Epitaxial-Strain-Induced Multiferroicity in $SrMnO_3$ from First Principles. *Phys. Rev. Lett.* **2010**, *104*, 207204:1–4.

(5) Hong, J.; Stroppa, A.; Íñiguez, J.; Picozzi, S.; Vanderbilt, D. Spin-phonon Coupling Effects in Transition-metal Perovskites: A DFT + U and Hybrid-functional Study. *Phys. Rev. B* **2012**, *85*, 054417:1–12.

(6) Patel, F.; Patel, S. $La_{1-x}Sr_xCoO_3$ (x=0, 0.2) Perovskites Type Catalyst for Carbon Monoxide Emission Control from Auto-Exhaust. *Procedia Eng.* **2013**, *51*, 324 – 329.

(7) Xiang, X.-P.; Zhao, L.-H.; Teng, B.-T.; Lang, J.-J.; Hu, X.; Li, T.; Fang, Y.-A.; Luo, M.-F.; Lin, J.-J. Catalytic Combustion of Methane on $La_{1-x}Ce_xFeO_3$ Oxides. *Appl. Surf. Sci.* **2013**, *276*, 328–332.

(8) Civera, A.; Pavese, M.; Saracco, G.; Specchia, V. Combustion Synthesis of Perovskite-type Catalysts for Natural Gas Combustion. *Catal. Today* **2003**, *83*, 199 – 211.

(9) Gallucci, K.; Villa, P.; Groppi, G.; Usberti, N.; Marra, G. Catalytic Combustion of Methane on $BaZr_{1-x}Me_xO_3$ Perovskites Synthesised by a Modified Citrate Method. *Catal. Today* **2012**, *197*, 236 – 242.

(10) Kim, C. H.; Qi, G.; Dahlberg, K.; Li, W. Strontium-doped Perovskites Rival Platinum Catalysts for Treating NOx in Simulated Diesel Exhaust. *Science* **2010**, *327*, 1624–1627.

(11) Martinelli, D. M.; Melo, D. M.; Pedrosa, A. M. G.; Martinelli, A. E.; Melo, M. A. d. F.; Batista, M. K.; Bitencourt, R. C. Use of Perovskite-Type Lanthanum Nickelate Synthesized by the Polymeric Precursor Method in the Steam Reforming Reaction of Methane. *Mater. Sci. Appl.* **2012**, *3*, 363–368.

(12) Thursfield, A.; Murugan, A.; Franca, R.; Metcalfe, I. S. Chemical looping and oxygen permeable ceramic membranes for hydrogen production–a review. *Energy Environ. Sci.* **2012**, *5*, 7421–7459.

(13) Jalili, H.; Han, J. W.; Kuru, Y.; Cai, Z.; Yildiz, B. New Insights into the Strain Coupling to Surface Chemistry, Electronic Structure, and Reactivity of $La_{0.7}Sr_{0.3}MnO_3$. *J. Phys. Chem. Lett.* **2011**, *2*, 801–807.

(14) Cai, Z.; Kuru, Y.; Han, J. W.; Chen, Y.; Yildiz, B. Surface Electronic Structure Transitions at High Temperature on Perovskite Oxides: The Case of Strained $La_{0.8}Sr_{0.2}CoO_3$ Thin Films. *J. Am. Chem. Soc.* **2011**, *133*, 17696–17704.

(15) Leion, H.; Larring, Y.; Bakken, E.; Bredesen, R.; Mattisson, T.; Lyngfelt, A. Use of $CaMn_{0.875}Ti_{0.125}O_3$ as Oxygen Carrier in Chemical-Looping with Oxygen Uncoupling. *Ener. Fuels* **2009**, *23*, 5276–5283.

(16) Galinsky, N. L.; Huang, Y.; Shafiefarhood, A.; Li, F. Iron Oxide with Facilitated O^{2-} Transport for Facile Fuel Oxidation and CO_2 Capture in a Chemical Looping Scheme. *ACS Sustainable Chem. Eng.* **2013**, *1*, 364–373.

(17) Jerndal, E.; Mattisson, T.; Lyngfelt, A. Thermal Analysis of Chemical-Looping Combustion. *Chem. Eng. Res. Des.* **2006**, *84*, 795 – 806.

(18) Hossain, M. M.; de Lasa, H. I. Chemical-looping Combustion (CLC) for Inherent Separations - A Review. *Chem. Eng. Sci.* **2008**, *63*, 4433 – 4451.

(19) Pishahang, M.; Bakken, E.; Stølen, S.; Larring, Y.; Thomas, C. I. Oxygen Nonstoichiometry and Redox Thermodynamics of $LaMn_{1-x}Co_xO$. *Solid State Ion.* **2013**, *231*, 49 – 57.

(20) Mizusaki, J. Nonstoichiometry, Diffusion, and Electrical Properties of Perovskite-Type Oxide Electrode Materials. *Solid State Ion.* **1992**, *52*, 79–91.

(21) Stølen, S.; Bakken, E.; Mohn, C. E. Oxygen-Deficient Perovskites: Linking Structure, Energetics and Ion Transport. *Phys. Chem. Chem. Phys.* **2006**, *8*, 429–447.

(22) Daturi, M.; Busca, G.; Willey, R. J. Surface and Structure Characterization of Some Perovskite-type Powders to be Used as Combustion Catalysts. *Chem. Mater.* **1995**, *7*, 2115–2126.

(23) Batiot-Dupeyrat, C.; Martinez-Ortega, F.; Ganne, M.; Tatibouët, J. Methane Catalytic Combustion on La-based Perovskite Type Catalysts in High Temperature Isothermal Conditions. *Appl. Catal., A* **2001**, *206*, 205–215.

(24) Orlyk, S.; Kantserova, M.; Shashkova, T.; Gubareni, E.; Chedryk, V.; Soloviev, S. Structure and Size Effects on the Catalytic Properties of Complex Metal Oxide Compositions in the Oxidative Conversion of Methane. *Theor. Exp. Chem.* **2013**, *49*, 22–34.

(25) Lisi, L.; Bagnasco, G.; Ciambelli, P.; Rossi, S. D.; Porta, P.; Russo, G.; Turco, M. Perovskite-Type Oxides: II. Redox Properties of $LaMn_{1-x}Cu_xO_3$ and $LaCo_{1-x}Cu_xO_3$ and Methane Catalytic Combustion. *J. Solid State Chem.* **1999**, *146*, 176 – 183.

(26) Wu-Laitao Luo, Y.; Liu, W. Combustion Synthesis and Characterization of Porous Perovskite Catalysts. *J. Chem. Sci.* **2007**, *119*, 237–241.

(27) Chiba, R.; Yoshimura, F.; Sakurai, Y. An Investigation of $LaNi_{1-x}Fe_xO_3$ as a Cathode Material for Solid Oxide Fuel Cells. *Solid State Ion.* **1999**, *124*, 281 – 288.

(28) Jiang, S. P.; Liu, L.; Ong, K. P.; Wu, P.; Li, J.; Pu, J. Electrical Conductivity and Performance of Doped $LaCrO_3$ Perovskite Oxides for Solid Oxide Fuel Cells. *J. Power Sources* **2008**, *176*, 82 – 89.

(29) Kuhn, J. N.; Matter, P. H.; Millet, J.-M. M.; Watson, R. B.; Ozkan, U. S. Oxygen Exchange Kinetics over Sr- and Co-Doped $LaFeO_3$. *J. Phys. Chem. C* **2008**, *112*, 12468–12476.

(30) Piskunov, S.; Heifets, E.; Jacob, T.; Kotomin, E. A.; Ellis, D. E.; Spohr, E. Electronic Structure and Thermodynamic Stability of $LaMnO_3$ and $La_{1-x}Sr_xMnO_3$ (001) Surfaces: *Ab initio* Calculations. *Phys. Rev. B* **2008**, *78*, 121406:1–4.

(31) Marchetti, L.; Forni, L. Catalytic Combustion of Methane over Perovskites. *Appl. Catal. B-Environ.* **1998**, *15*, 179 – 187.

(32) Saracco, G.; Scibilia, G.; Iannibello, A.; Baldi, G. Methane Combustion on Mg-doped $LaCrO_3$ Perovskite Catalysts. *Appl. Catal. B-Environ.* **1996**, *8*, 229 – 244.

(33) Tian, T.; Zhan, M.; Wang, W.; Chen, C. Surface Properties and Catalytic Performance in Methane Combustion of $La_{0.7}Sr_{0.3}Fe_{1-y}Ga_yO_{3-\delta}$ Perovskite-type Oxides. *Catal. Commun.* **2009**, *10*, 513 – 517.

(34) Lee, Y.-L.; Kleis, J.; Rossmeisl, J.; Morgan, D. *Ab initio* Energetics of $LaBO_3$(001) (B = Mn, Fe, Co, and Ni) for Solid Oxide Fuel Cell Cathodes. *Phys. Rev. B* **2009**, *80*, 224101:1–20.

(35) Pavone, M.; Ritzmann, A. M.; Carter, E. A. Quantum-mechanics-based Design Principles for Solid Oxide Fuel Cell Cathode Materials. *Energy Environ. Sci.* **2011**, *4*, 4933–4937.

(36) Benedetto, A. D.; Landi, G.; Sarli, V. D.; Barbato, P.; Pirone, R.; Russo, G. Methane Catalytic Combustion Under Pressure. *Catal. Today* **2012**, *197*, 206–213.

(37) Barbato, P.; Landi, G.; Russo, G. Catalytic Combustion of CH_4-H_2-CO Mixtures at Pressure Up to 10 bar. *Fuel Process. Technol.* **2013**, *107*, 147–154.

(38) Arai, H.; Yamada, T.; Eguchi, K.; Seiyama, T. Catalytic Combustion of Methane over Various Perovskite-type Oxides. *Appl. Catal.* **1986**, *26*, 265 – 276.

(39) Seim, H.; Fjellvâg, H. Non-Stoichiometric $LaVO_3$. I. Synthesis and Physical Properties. *Acta Chem. Scand.* **1998**, *52*, 1096 – 1103.

(40) Spinicci, R.; Tofanari, A.; Delmastro, A.; Mazza, D.; Ronchetti, S. Catalytic Properties of Stoichiometric and Non-stoichiometric $LaFeO_3$ Perovskite for Total Oxidation of Methane. *Mater. Chem. Phys.* **2002**, *76*, 20 – 25.

(41) Cherry, M.; Islam, M.; Catlow, C. Oxygen Ion Migration in Perovskite-Type Oxides. *J. Solid State Chem.* **1995**, *118*, 125 – 132.

(42) Lee, Y. N.; Lago, R. M.; Fierro, J. L. G.; Cortés, V.; Sapina, F.; Martínez, E. Surface Properties and Catalytic Performance for Ethane Combustion of $La_{1-x}K_xMnO_{3+\delta}$ Perovskites. *Appl. Catal., A* **2001**, *207*, 17 – 24.

(43) Seiyama, T. Total Oxidation of Hydrocarbons on Perovskite Oxides. *Catal. Rev.* **1992**, *34*, 281–300.

(44) Kuhn, J. N.; Ozkan, U. S. Effect of Co Content Upon the Bulk Structure of Sr- and Co-doped $LaFeO_3$. *Catal. Lett.* **2008**, *121*, 179–188.

(45) Sundell, P. G.; Björketun, M. E.; Wahnström, G. Thermodynamics of Doping and Vacancy Formation in $BaZrO_3$ Perovskite Oxide from Density Functional Calculations. *Phys. Rev. B* **2006**, *73*, 104112:1–10.

(46) Huang, W. L.; Zhu, Q.; Ge, W.; Li, H. Oxygen-vacancy Formation in $LaMO_3$ (M = Ti, V, Cr, Mn, Fe, Co, Ni) Calculated at Both GGA and GGA + U Levels. *Comp. Mater. Sci.* **2011**, *50*, 1800 – 1805.

(47) Zeng, Z.; Calle-Vallejo, F.; Mogensen, M. B.; Rossmeisl, J. Generalized Trends in the Formation Energies of Perovskite Oxides. *Phys. Chem. Chem. Phys.* **2013**, *15*, 7526–7533.

(48) Akhade, S. A.; Kitchin, J. R. Effects of Strain, d-band Filling, and Oxidation State on the Surface Electronic Structure and Reactivity of 3d Perovskite Surfaces. *J. Chem. Phys.* **2012**, *137*, 084703:1–9.

(49) Wang, L.; Maxisch, T.; Ceder, G. Oxidation Energies of Transition Metal Oxides within the GGA + U Framework. *Phys. Rev. B* **2006**, *73*, 195107:1–6.

(50) Zhou, F.; Cococcioni, M.; Marianetti, C. A.; Morgan, D.; Ceder, G. First-principles Prediction of Redox Potentials in Transition-metal Compounds with LDA + U. *Phys. Rev. B* **2004**, *70*, 235121:1–8.

(51) Cococcioni, M.; de Gironcoli, S. Linear Response Approach to the Calculation of the Effective Interaction Parameters in the LDA + U Method. *Phys. Rev. B* **2005**, *71*, 035105:1–16.

(52) Grindy, S.; Meredig, B.; Kirklin, S.; Saal, J. E.; Wolverton, C. Approaching Chemical Accuracy with Density Functional Calculations: Diatomic Energy Corrections. *Phys. Rev. B* **2013**, *87*, 075150:1–8.

(53) Nakamura, T.; Petzow, G.; Gauckler, L. Stability of the Perovskite Phase $LaBO_3$ (B = V, Cr, Mn, Fe, Co, Ni) in Reducing Atmosphere I. Experimental Results. *Mater. Res. Bull.* **1979**, *14*, 649 – 659.

(54) May, S. J.; Kim, J.-W.; Rondinelli, J. M.; Karapetrova, E.; Spaldin, N. A.; Bhattacharya, A.; Ryan, P. J. Quantifying Octahedral Rotations in Strained Perovskite Oxide Films. *Phys. Rev. B* **2010**, *82*, 014110:1–7.

(55) Vailionis, A.; Boschker, H.; Siemons, W.; Houwman, E. P.; Blank, D. H. A.; Rijnders, G.; Koster, G. Misfit Strain Accommodation in Epitaxial ABO_3 Perovskites: Lattice Rotations and Lattice Modulations. *Phys. Rev. B* **2011**, *83*, 064101:1–10.

(56) Wollan, E. O.; Koehler, W. C. Neutron Diffraction Study of the Magnetic Properties of the Series of Perovskite-Type Compounds $[(1-x)\mathrm{La},\ x\mathrm{Ca}]\mathrm{MnO}_3$. *Phys. Rev.* **1955**, *100*, 545–563.

(57) Pishahang, M.; Mohn, C. E.; Stølen, S.; Bakken, E. DFT-study of the Energetics of Perovskite-type Oxides $LaMO_3$ (M = Sc-Cu). *RSC Adv.* **2012**, *2*, 10667–10672.

(58) Ravindran, P.; Vidya, R.; Fjellvåg, H.; Kjekshus, A. Electronic Structure and Excited-state Properties of Perovskite-like Oxides. *J. Crys. Growth* **2004**, *268*, 554 – 559.

(59) Bhattacharya, A.; May, S. J.; te Velthuis, S. G. E.; Warusawithana, M.; Zhai, X.; Jiang, B.; Zuo, J.-M.; Fitzsimmons, M. R.; Bader, S. D.; Eckstein, J. N. Metal-Insulator Transition and Its Relation to Magnetic Structure in $(LaMnO_3)_{2n}/(SrMnO_3)_n$ Superlattices. *Phys. Rev. Lett.* **2008**, *100*, 257203:1–4.

(60) Chevrier, V. L.; Ong, S. P.; Armiento, R.; Chan, M. K. Y.; Ceder, G. Hybrid Density Functional Calculations of Redox Potentials and Formation Energies of Transition Metal Compounds. *Phys. Rev. B* **2010**, *82*, 075122:1–11.

(61) Kresse, G.; Furthmüller, J. Efficient Iterative Schemes for *ab initio* Total-energy Calculations Using a Plane-wave Basis Set. *Phys. Rev. B* **1996**, *54*, 11169–11186.

(62) Kresse, G.; Joubert, D. From Ultrasoft Pseudopotentials to the Projector Augmented-wave Method. *Phys. Rev. B* **1999**, *59*, 1758–1775.

(63) Perdew, J. P.; Burke, K.; Ernzerhof, M. Generalized Gradient Approximation Made Simple. *Phys. Rev. Lett.* **1996**, *77*, 3865–3868.

(64) Blöchl, P. E. Projector Augmented-wave Method. *Phys. Rev. B* **1994**, *50*, 17953–17979.

(65) Monkhorst, H. J.; Pack, J. D. Special Points for Brillouin-zone Integrations. *Phys. Rev. B* **1976**, *13*, 5188–5192.

(66) Murnaghan, F. D. The Compressibility of Media under Extreme Pressures. *Proc. Natl. Acad. Sci. U. S. A.* **1944**, *30*, 244–247.

(67) Roosmalen, J. V.; Cordfunke, E. A New Defect Model to Describe the Oxygen Deficiency in Perovskite-type Oxides. *J. Solid State Chem.* **1991**, *93*, 212 – 219.

(68) Yang, Z.; Luo, G.; Lu, Z.; Hermansson, K. Oxygen Vacancy Formation Energy in Pd-doped Ceria: A DFT + U Study. *J. Chem. Phys.* **2007**, *127*, 074704:1–5.

(69) Foster, A. S.; Lopez Gejo, F.; Shluger, A. L.; Nieminen, R. M. Vacancy and Interstitial Defects in Hafnia. *Phys. Rev. B* **2002**, *65*, 174117:1–13.

(70) Readman, J. E.; Olafsen, A.; Larring, Y.; Blom, R. $La_{0.8}Sr_{0.2}Co_{0.2}Fe_{0.8}O_3$ - as a Potential Oxygen Carrier in a Chemical Looping Type Reactor, an In-situ Powder X-ray Diffraction Study. *J. Mater. Chem.* **2005**, *15*, 1931–1937.

(71) Senaris-Rodríguez, M.; Goodenough, J. $LaCoO_3$ Revisited. *J. Solid State Chem.* **1995**, *116*, 224 – 231.

(72) Norby, P.; Andersen, I.; Andersen, E.; Andersen, N. The Crystal Structure of Lanthanum Manganate(iii), $LaMnO_3$, at Room Temperature and at 1273 K under N_2. *J. Solid State Chem.* **1995**, *119*, 191 – 196.

(73) Haas, O.; Struis, R.; McBreen, J. Synchrotron X-ray Absorption of $LaCoO_3$ Perovskite. *J. Solid State Chem.* **2004**, *177*, 1000 – 1010.

(74) Khattak, C.; Cox, D. Structural Studies of the (La,Sr)CrO_3 System. *Mater. Res. Bull.* **1977**, *12*, 463 – 471.

(75) Aroyo, M. I.; Perez-Mato, J. M.; Capillas, C.; Kroumova, E.; Ivantchev, S.; Madariaga, G.; Kirov, A.; Wondratschek, H. Bilbao Crystallographic Server: I. Databases and Crystallographic Computing Programs. *Z. Kristallogr.* **2006**, *221*, 15–27.

(76) Vosko, S. H.; Wilk, L.; Nusair, M. Accurate Spin-dependent Electron Liquid Correlation Energies for Local Spin Density Calculations: A Critical Analysis. *Can. J. Phys.* **1980**, *58*, 1200–1211.

(77) Liechtenstein, A. I.; Anisimov, V. I.; Zaanen, J. Density-functional Theory and Strong Interactions: Orbital Ordering in Mott-Hubbard Insulators. *Phys. Rev. B* **1995**, *52*, R5467–R5470.

(78) Kulik, H. J.; Marzari, N. A Self-consistent Hubbard U Density-functional Theory Approach to the Addition-elimination Reactions of Hydrocarbons on Bare FeO^+. *J. Chem. Phys.* **2008**, *129*, 134314:1–12.

(79) Jain, A.; Hautier, G.; Ong, S. P.; Moore, C. J.; Fischer, C. C.; Persson, K. A.; Ceder, G. Formation Enthalpies by Mixing GGA and GGA + U Calculations. *Phys. Rev. B* **2011**, *84*, 045115:1–10.

(80) Kulik, H. J.; Marzari, N. Systematic Study of First-row Transition-metal Diatomic Molecules: A Self-consistent DFT + U Approach. *J. Chem. Phys.* **2010**, *133*, 114103:1–16.

(81) Czyżk, M. T.; Sawatzky, G. A. Local-density Functional and On-site Correlations: The Electronic Structure of La_2CuO_4 and $LaCuO_3$. *Phys. Rev. B* **1994**, *49*, 14211–14228.

(82) Okamoto, S.; Millis, A. J.; Spaldin, N. A. Lattice Relaxation in Oxide Heterostructures: $LaTiO_3/SrTiO_3$ Superlattices. *Phys. Rev. Lett.* **2006**, *97*, 056802:1–4.

(83) Gou, G.; Grinberg, I.; Rappe, A. M.; Rondinelli, J. M. Lattice Normal Modes and Electronic Properties of the Correlated Metal $LaNiO_3$. *Phys. Rev. B* **2011**, *84*, 144101:1–13.

(84) Hsu, H.; Blaha, P.; Wentzcovitch, R. M. Ferromagnetic Insulating State in Tensile-strained $LaCoO_3$ Thin Films from LDA + U Calculations. *Phys. Rev. B* **2012**, *85*, 140404(R):1–5.

(85) Dudarev, S. L.; Botton, G. A.; Savrasov, S. Y.; Humphreys, C. J.; Sutton, A. P. Electron-energy-loss Spectra and the Structural Stability of Nickel Oxide: An LSDA+U Study. *Phys. Rev. B* **1998**, *57*, 1505–1509.

(86) Giannozzi, P.; Baroni, S.; Bonini, N.; Calandra, M.; Car, R.; Cavazzoni, C.; Ceresoli, D.; Chiarotti, G. L.; Cococcioni, M.; Dabo, I. et al. QUANTUM ESPRESSO: A Modular and Open-source Software Project for Quantum Simulations of Materials. *J. Phys.: Condens. Matter* **2009**, *21*, 395502:1–19.

(87) Li, X.; Zhao, H.; Gao, F.; Chen, N.; Xu, N. La and Sc Co-doped $SrTiO_3$ as Novel Anode Materials for Solid Oxide Fuel Cells. *Electrochem. Commun.* **2008**, *10*, 1567 – 1570.

(88) Costa, G. A.; Kaiser, E. Structural and Thermal Properties of the Alkaline Cuprate $KCuO_2$. *Thermochim. Acta* **1995**, *269 - 270*, 591 – 598.

(89) Calle-Vallejo, F.; Inoglu, N. G.; Su, H.-Y.; Martinez, J. I.; Man, I. C.; Koper, M. T. M.; Kitchin, J. R.; Rossmeisl, J. Number of Outer Electrons as Descriptor for Adsorption Processes on Transition Metals and their Oxides. *Chem. Sci.* **2013**, *4*, 1245–1249.

(90) Sayre, J. D.; Delaney, K. T.; Spaldin, N. A. Interplay between Strain and Oxygen Vacancies in Lanthanum Aluminate. *arXiv.org, Condens. Matter* **2012**, 1202.1431.

(91) Lento, J.; Mozos, J.-L.; Nieminen, R. M. Charged Point Defects in Semiconductors and the Supercell Approximation. *J. Phys.: Condens. Matter* **2002**, *14*, 2637 – 2645.

(92) Geller, S.; Raccah, P. M. Phase Transitions in Perovskite-like Compounds of the Rare Earths. *Phys. Rev. B* **1970**, *2*, 1167–1172.

(93) Geller, S. Crystallographic Studies of Perovskite-like Compounds. IV. Rare Earth Scandates, Vanadites, Galliates, Orthochromites. *Acta Crystallogr.* **1957**, *10*, 243–248.

(94) De Raychaudhury, M.; Pavarini, E.; Andersen, O. K. Orbital Fluctuations in the Different Phases of $LaVO_3$ and YVO_3. *Phys. Rev. Lett.* **2007**, *99*, 126402:1–4.

(95) Kulik, H. J.; Marzari, N. Accurate Potential Energy Surfaces with a DFT+U(R) Approach. *J. Chem. Phys.* **2011**, *135*, 194105:1–10.

(96) Kulik, H. J.; Cococcioni, M.; Scherlis, D. A.; Marzari, N. Density Functional Theory in Transition-Metal Chemistry: A Self-Consistent Hubbard U Approach. *Phys. Rev. Lett.* **2006**, *97*, 103001:1–4.
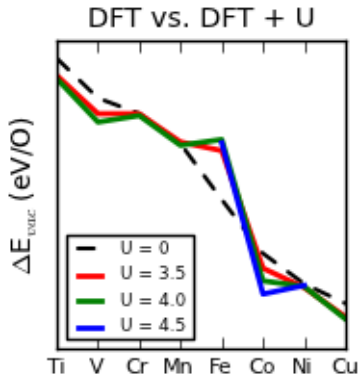
For Table of Contents Only